

ARTICLE

DCX-EMAP is a core organizer for the ultrastructure of *Drosophila* mechanosensory organelles

Xuewei Song¹, Lihong Cui¹, Menghua Wu¹, Shan Wang¹, Yinlong Song¹, Zhen Liu¹, Zhaoyu Xue¹, Wei Chen¹, Yingjie Zhang¹, Hui Li¹, Landi Sun^{1,2}, and Xin Liang¹

Mechanoreceptor cells develop specialized mechanosensory organelles (MOs), where force-sensitive channels and supporting structures are organized in an orderly manner to detect forces. It is intriguing how MOs are formed. Here, we address this issue by studying the MOs of fly ciliated mechanoreceptors. We show that the main structure of the MOs is a compound cytoskeleton formed of short microtubules and electron-dense materials (EDMs). In a knock-out mutant of *DCX-EMAP*, this cytoskeleton is nearly absent, suggesting that *DCX-EMAP* is required for the formation of the MOs and in turn fly mechanotransduction. Further analysis reveals that *DCX-EMAP* expresses in fly ciliated mechanoreceptors and localizes to the MOs. Moreover, it plays dual roles by promoting the assembly/stabilization of the microtubules and the accumulation of the EDMs in the MOs. Therefore, *DCX-EMAP* serves as a core ultrastructural organizer of the MOs, and this finding provides novel molecular insights as to how fly MOs are formed.

Introduction

Mechanoreceptor cells start the neural pathway of mechanosensation by converting physical stimuli (e.g., force or deformation) into cellular signals (Chalfie, 2009). To accomplish this task, they develop specialized mechanosensory organelles (MOs), which are structural-mechanical entities that consist of force-sensitive channels and supporting components, such as the cytoskeleton and extracellular matrix (Gillespie and Walker, 2001; Lumpkin et al., 2010). While force-sensitive ion channels are key signal transducers, supporting components were thought to refine the sensory features of mechanoreceptor cells (e.g., sensitivity and dynamic range). For example, vertebrate inner ear hair cells grow stereocilia that contain intracellular actin bundles and extracellular tip-links, which serve to match the mechanical impedance when stereocilia deflection is converted into a conformational change of the mechanotransduction channels (Gillespie and Müller, 2009). The touch receptors of *C. elegans* form a specialized sensory complex containing the extracellular matrix (e.g., MEC-5), membrane channels (MEC-4 and MEC-10), and 15-protofilament microtubules (MEC-7 and MEC-12) to sense tactile signals (Goodman, 2006; Lumpkin et al., 2010). Recent studies suggest that Piezo, a force-sensitive channel that contributes to the perception of various mechanical stimuli, may be tethered to and regulated by F-actin in cells (Wang et al., 2022). Therefore, MOs are structurally specialized to match the sensory modality of the

mechanoreceptors. This raises the question of how the MOs are formed.

The MOs of *Drosophila* ciliated mechanoreceptors (i.e., type I mechanoreceptors) have been extensively studied to understand the structural basis of mechanotransduction (Keil, 1997; Liang et al., 2013; Sun et al., 2019, 2021). Early ultrastructural analysis showed that the main intracellular structure of the MOs is a compound cytoskeletal structure consisting of arrayed microtubules and electron-dense materials (EDMs; Keil, 1997). Later, it was shown that NompC force-sensitive channels are structurally linked to the microtubules and also formed into arrays in the MO membrane (Sun et al., 2019). These observations suggest that the entire MO acts as an integrated mechanosensor with a nanoscopic size. In our recent work, we revealed that short microtubules are required for the formation of the MOs and that the “kat-60LI/Patronin” module is required to generate the short microtubules (Sun et al., 2021). An ensuing question is how these short microtubules are stabilized and organized in the MOs.

We previously showed that knocking down the expression level of Patronin, a microtubule minus-end-stabilizing protein (Goodwin and Vale, 2010; Hendershott and Vale, 2014), reduces the amount of the MO microtubules (Sun et al., 2021), suggesting that Patronin stabilizes the MO microtubules. However, we also found that in addition to Patronin, there is a MO-specific

¹IDG/McGovern Institute for Brain Research, School of Life Sciences, Tsinghua University, Beijing, China; ²Guangzhou Laboratory, Guangzhou, China.

Correspondence to Xin Liang: xinliang@tsinghua.edu.cn; Landi Sun: sunlandi.2015@tsinghua.org.cn.

© 2023 Song et al. This article is distributed under the terms of an Attribution-Noncommercial-Share Alike-No Mirror Sites license for the first six months after the publication date (see <http://www.rupress.org/terms/>). After six months it is available under a Creative Commons License (Attribution-Noncommercial-Share Alike 4.0 International license, as described at <https://creativecommons.org/licenses/by-nc-sa/4.0/>).

microtubule-stabilizing mechanism (Sun et al., 2021). A previous study showed that DCX-EMAP, a doublecortin (DCX) domain-containing protein, is highly enriched in fly haltere tissue based on the DNA array analysis (Bechstetd et al., 2010) and that a piggyBac insertion mutant of DCX-EMAP, which may express a truncated protein (Liang et al., 2014), contains a disrupted microtubule array in the outer segment of campaniform mechanoreceptors. This implies that DCX-EMAP may be key for the assembly or stability of microtubules inside the mechanosensory cilia. However, due to the lack of further genetic and cell biological analysis, the cellular functions and biochemical mechanism of DCX-EMAP remain elusive, especially in the context of the recently resolved structure of the mechanosensory cilia (Sun et al., 2021).

DCX-EMAP belongs to the EMAP (echinoderm-microtubule-associated proteins) family, the members of which are regulators for microtubule dynamics (Brisch et al., 1996; Eichenmuller et al., 2002; Hamill et al., 1998; Pollmann et al., 2006). All EMAP proteins share a conserved TAPE (tandem atypical propeller in EMLs) domain at the carboxyl-terminal, including the HELP (hydrophobic echinoderm-microtubule-associated-like protein) domain and multiple WD40 repeats. The amino-terminal part of EMAP proteins often contains a coiled-coil domain that binds to microtubules through trimerization (Fry et al., 2016; Hueston et al., 2008), but see Hotta et al. (2022). Among all EMAP family members, DCX-EMAP is unique because the coiled-coil domain is replaced by a tandem of two DCX domains (Bechstetd et al., 2010), which has a microtubule-binding/stabilizing activity (Moores et al., 2004, 2006). It was found that the DCX-domain-containing (DCDC) proteins express in a wide range of cells and show diverse cellular functions (Deuel et al., 2006; Francis et al., 1999; Gleeson et al., 1999). Therefore, it is intriguing to understand how DCX-EMAP couples the functions of the DCX and EMAP families in a specific cellular process, such as the formation of a modified cilium.

In the present work, we study the formation of fly MOs by analyzing the cellular functions of DCX-EMAP, an essential molecule for fly mechanosensation. Our results show that DCX-EMAP specifically expresses in fly mechanosensory cilia and acts as a core organizer for the ultrastructure of the MOs, thereby having a direct contribution to fly mechanotransduction. These findings help take an important step forward in understanding how fly MOs are formed. In the meantime, this study provides implications to understand the cellular roles of the DCDC and EMAP family members in ciliary assembly and maintenance.

Results

The MOs of fly mechanoreceptors have an ordered ultrastructure

In the present study, we used campaniform mechanoreceptors in fly haltere (fly's gyroscopes) and leg as our model cells (Fig. 1, A and B). In haltere, campaniform receptors were arrayed in the pedicel and scabellum segments, while in the leg, individual receptors were found at the joint of leg segments (Fig. 1 B). Despite being in different organs, the sensory neurons in haltere

and leg receptors shared a similar cellular organization. Both are bipolar neurons with a modified cilium at the distal end of the dendrite. The distal part of the modified cilium is called the outer segment (Fig. 1 B). The previous tomographic reconstruction showed that the outer segment (OS) of fly campaniform mechanoreceptors can be further divided into two compartments, i.e., a tubular body (TB) and a mechanosensory organelle (MO; Sun et al., 2021; Fig. 1, C and D; and Video 1). In the MO, hundreds of "NompC-microtubule" complexes, each of which is thought to be an elementary mechanotransduction apparatus, are arranged in an orderly manner (Sun et al., 2019). This raises a question of how the MOs are organized.

To address this issue, we characterized the ultrastructural organization of the MOs using electron tomography (ET). In fly haltere pedicel campaniform mechanoreceptors, the MOs had a round-ended rectangular shape in which the microtubules were arranged into two parallel rows (Fig. 1, D and E). Within each row, the microtubules were further clustered into smaller arrays consisting of mostly three to eight microtubules with an intermicrotubule distance of 26 ± 1 nm (d_1 , center-to-center distance, $n = 326$ microtubule pairs in three cells) and the interarray distance (d_2) of 46 ± 8 nm ($n = 156$ microtubule pairs in three cells; Fig. 1, E and F). In leg receptors, microtubules were embedded in the EDMs and formed a 3D array that fitted into the dome-shaped MO (Fig. 1, G and I; and Video 2). In this array, the intermicrotubule distance was 44 ± 6 nm ($n = 442$ microtubule pairs in three cells; Fig. 1 J), similar to d_2 in the haltere receptors.

In both haltere and leg receptors, the space between microtubules or microtubule arrays was filled with the electron-dense materials (EDMs; Fig. 1, D, E, H, and I) and the EDMs directly deposited on microtubule walls to form a 3D porous structure (Fig. 1, E and I; and Fig. S1), suggesting their direct interaction with the MO microtubules. The structural resemblance suggests that the compound cytoskeletal structures in the MOs of arrayed (haltere) and isolate (leg) mechanoreceptors might share common molecular components and probably a similar assembly mechanism.

DCX-EMAP is required for fly mechanotransduction

Having resolved the 3D structure of the MO, we then set out to understand how the compound cytoskeleton in the MOs is stabilized and organized. Among all the molecules known to express in fly type I mechanoreceptors, DCX-EMAP is thought to be a microtubule-stabilizing factor. Moreover, the carboxyl end of DCX-EMAP contains a TAPE domain, a known structural platform for protein-protein interactions. The multidomain nature of DCX-EMAP implies that it may act as a stabilizer and organizer for microtubules in vivo.

To fully explore the role of DCX-EMAP, we first generated a set of tool strains (Fig. 2 A, see Materials and methods), including a promoter-gal4 driver (*DCX-EMAP-gal4*), a GFP knock-in strain (*DCX-EMAP^{KI}*), a genomic knock-out mutant (*DCX-EMAP^{KO}*), and two transgenic lines that carried the coding sequence of *DCX-EMAP* with or without the amino-terminal GFP fusion (*uas-gfp-DCX-EMAP* and *uas-DCX-EMAP*). Using a previously developed monoclonal antibody against DCX-EMAP (Fig. 2 A; Liang et al., 2014), we verified that the DCX-EMAP signal was

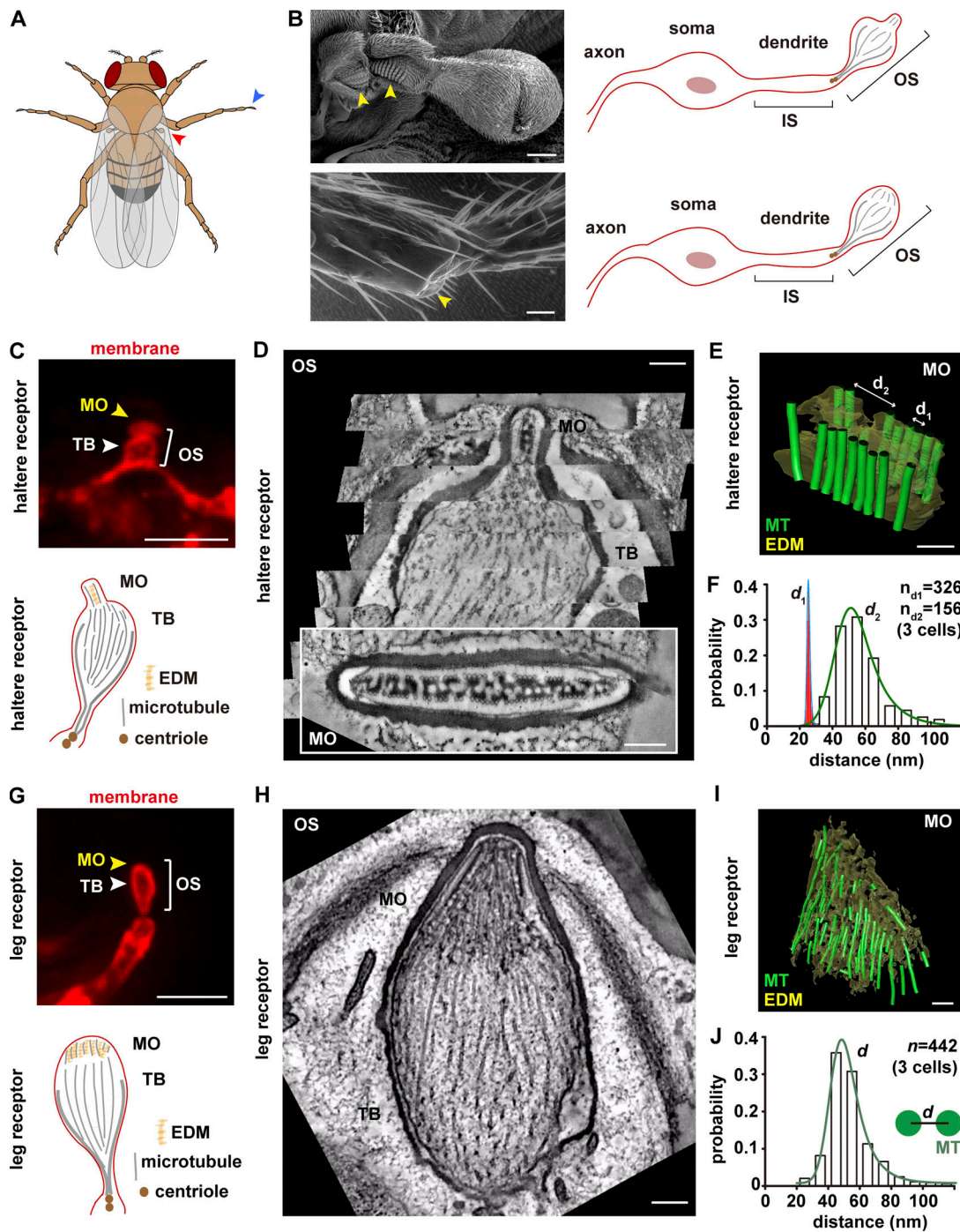


Figure 1. Ultrastructural organization of the MOs in fly campaniform mechanoreceptors. (A) Cartoon schematic of a fly. The red and blue arrowheads indicate the haltere and the tarsus of a leg, respectively. (B) Representative SEM images of haltere receptors (yellow arrowhead, upper panel) and a leg receptor (yellow arrowhead, lower panel). Scale bars, 30 μm (upper); 2 μm (lower). The cartoons on the right showed the cellular organization of the sensory neurons. OS, outer segment; IS, inner segment. (C) Lateral view of the outer segment of a haltere receptor and the corresponding cartoon schematic (lower panel). Genotype: *DCX-EMAP-gal4, uas-cd4-tdtom/+*. The OS, MO, and TB are indicated. Scale bar, 5 μm . (D) Lateral view (ET slice image) of the outer segment in a wild-type haltere receptor. Inset, cross-view of the MO. Scale bars, 300 nm. Also see [Video 1](#). (E) The reconstructed model of microtubules in the MO of a haltere receptor. Scale bar, 100 nm. d_1 , the inter-microtubule distance within the same array. d_2 , the inter-array distance. (F) Probability density distribution of d_1 and d_2 in haltere receptors. The number of microtubule pairs was indicated. (G) Lateral view of the outer segment (upper panel) of a leg receptor and the corresponding cartoon schematic (lower panel). Genotype: *DCX-EMAP-gal4, uas-cd4-tdtom/+*. The OS, MO, and TB are indicated. Scale bar, 5 μm . (H) Lateral view (ET slice image) of the outer segment in a wild-type leg receptor. Scale bar, 300 nm. Also see [Video 2](#). (I) Reconstructed model of microtubules in the MO of a leg receptor. Scale bar, 100 nm. d , the distance between adjacent microtubules. (J) Probability density distribution of d in leg receptors. d , the distance between adjacent microtubules. The number of microtubule pairs is indicated.

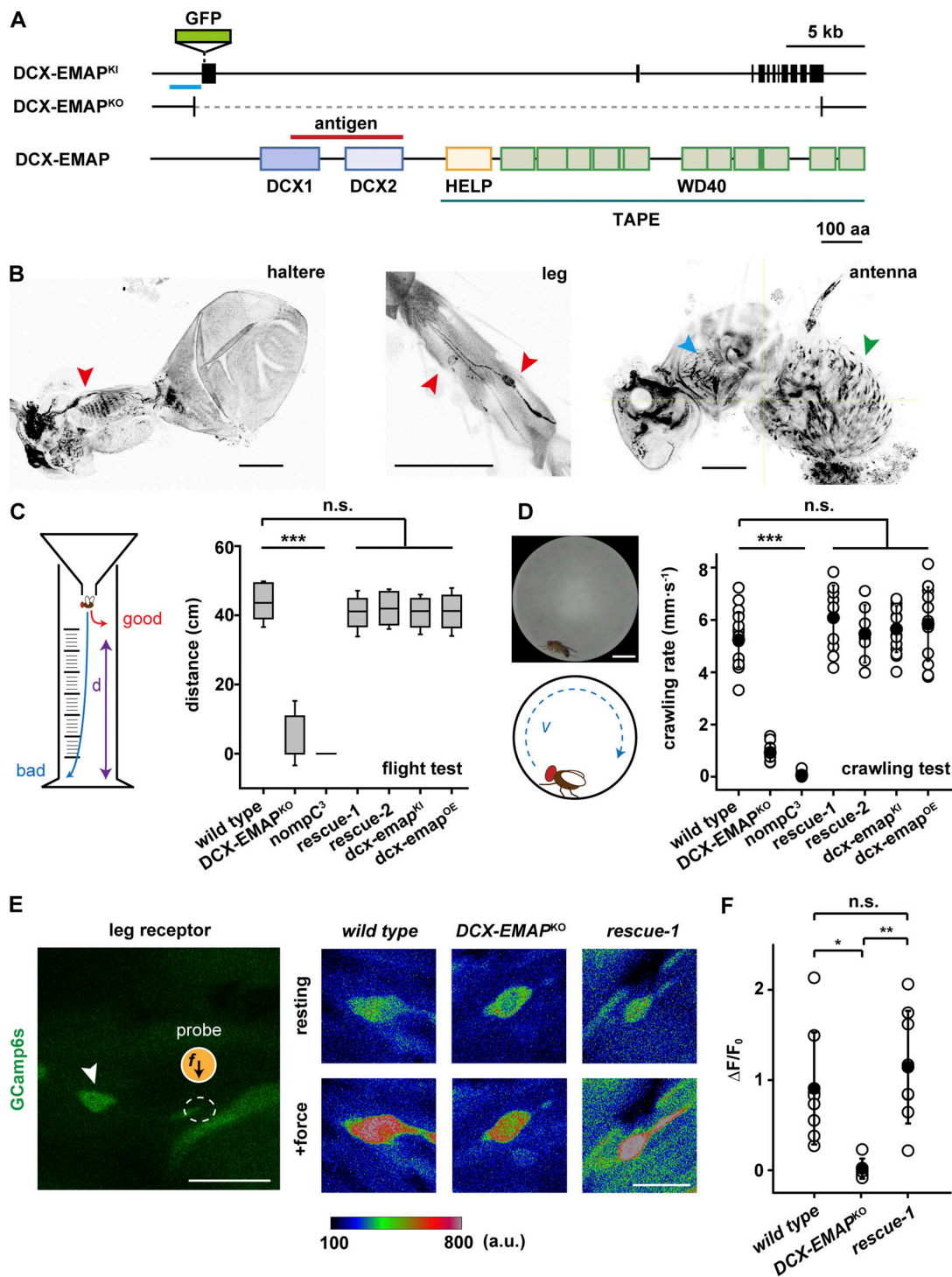


Figure 2. DCX-EMAP is required for fly mechanotransduction. (A) Schematic diagrams of *DCX-EMAP^{KI}*, *DCX-EMAP^{KO}*, and the domain organization of DCX-EMAP. The blue bar indicates the promoter sequence (1.5 kb) used to generate the *DCX-EMAP-gal4* strain. The red bar marks the fragment of DCX-EMAP (amino acids 258–461, 204 amino acids) used as the antigen to generate the DCX-EMAP antibody (Liang et al., 2014). (B) DCX-EMAP expressed in fly mechanosensory organs. Left: Haltere campaniform mechanoreceptors (red arrowhead). Middle: Leg campaniform and bristle mechanoreceptors (red arrowheads). Right: The Johnston's organ (blue arrowhead) and olfactory receptor cells (green arrowhead) in fly antenna (also see Fig. S2). Genotype: *DCX-EMAP-gal4; uas-cd4-tdgfp*. Scale bars, 50 μ m. (C) Flight tests of *wild type* ($n = 73$ flies), *DCX-EMAP^{KO}* ($n = 151$ flies), *nompC³* ($n = 18$ flies), two rescue strains (*rescue-1*: *DCX-EMAP-gal4/uas-gfp-DCX-EMAP; DCX-EMAP^{KO}*, $n = 71$ flies; *rescue-2*: *nompC-gal4/uas-gfp-DCX-EMAP; DCX-EMAP^{KO}*, $n = 42$ flies), *DCX-EMAP^{KI}* ($n = 66$ flies), and *DCX-EMAP^{OE}* (*DCX-EMAP-gal4/uas-gfp-DCX-EMAP*, $n = 54$ flies). The schematic for the assay is shown in the left panel. (D) Crawling tests of *wild type* ($n = 18$ flies), *DCX-EMAP^{KO}* ($n = 11$ flies), *nompC³* ($n = 13$ flies), two rescue strains (*rescue-1*: $n = 10$ flies; *rescue-2*: $n = 7$ flies), *DCX-EMAP^{KI}* ($n = 15$ flies), and *DCX-EMAP^{OE}* ($n = 12$ flies). The schematics for the assay are shown in the left panels. Scale bar, 2 mm. Also see Video 3. (E) Representative images of the in vivo calcium recording in *wild type* (*DCX-EMAP-gal4, uas-cd4-tdtom/uas-GCamp6s*), *DCX-EMAP^{KO}* (*DCX-EMAP-gal4, uas-cd4-tdtom/uas-GCamp6s; DCX-EMAP^{KO}*), and *rescue* (*DCX-EMAP-gal4, uas-cd4-tdtom, uas-DCX-EMAP/uas-GCamp6s; DCX-EMAP^{KO}*). Scale bar, 10 μ m. (F) Statistical quantification of the calcium responses. *Wild type* ($n = 8$ cells), *DCX-EMAP^{KO}* ($n = 6$ cells), and *rescue-1* ($n = 8$ cells). In D and F, data are presented as mean \pm SD with scattered data points. Two-sided unpaired Student's test. *, $P < 0.05$; **, $P < 0.01$; ***, $P < 0.001$; n.s., no significance.

absent in *DCX-EMAP^{KO}* and could be recovered by expressing the cDNA of *DCX-EMAP* (Fig. S2).

Using the promoter-*gal4* driver, we examined the expression pattern of *DCX-EMAP*. *DCX-EMAP* was primarily expressed in fly type I mechanoreceptor cells, such as external sensory cells (i.e., campaniform and bristle receptors) and chordotonal organs (e.g., the Johnson's organs and the larval *lch5*; Fig. 2 B and Fig. S2). We also looked into FlyCellAtlas and focused on the datasets of antenna, haltere, and leg tissues. In these tissues, the expression of *DCX-EMAP* was most prominent in mechanosensory cells (*nompC*-positive; Fig. S3). These observations imply that *DCX-EMAP* may play a role in mechanosensation.

Using the flight and crawling tests for the adult fly, we found that *DCX-EMAP^{KO}* had severe locomotion defects (Fig. 2, C and D; and Video 3). The behavioral phenotype was close to that observed in *nompC³* and stronger than that observed in the piggyBac insertion mutant of *DCX-EMAP* (*DCX-EMAP^{fo2665}*; Bechstedt et al., 2010; Fig. 2, C and D), suggesting that the function of *DCX-EMAP* has not yet been fully understood. Expressing *DCX-EMAP* using its own promoter (*DCX-EMAP-gal4*) or a known mechanoreceptor-specific driver (*nompC-gal4*) fully rescued the behavioral phenotypes (Fig. 2, C and D; and Video 3), suggesting that the behavioral phenotypes could be attributed to mechanosensory defects. Moreover, both *DCX-EMAP^{KI}* and *DCX-EMAP^{OE}* (OE; over-expression) strains showed normal locomotion behaviors, demonstrating that the genetic manipulations do not interfere the function of *DCX-EMAP* (Fig. 2, C and D). Finally, using a previously established functional assay that records the force-evoked calcium response of mechanosensory neurons (Sun et al., 2021), we showed that the cellular response of campaniform mechanoreceptors to mechanical stimuli was largely abolished in *DCX-EMAP^{KO}*, and this defect can be restored in the rescue strain (Fig. 2, E and F). Based on these results, we conclude that *DCX-EMAP* is required for fly mechanosensation.

In both our experimental observations and the FlyCellAtlas datasets, we noted some expression of *DCX-EMAP* in a small number of antenna olfactory receptors (Fig. 2 B and Fig. S3). However, further experiments using the *DCX-EMAP^{KI}* and *DCX-EMAP^{OE}* strains did not show a clear and consistent subcellular localization of *DCX-EMAP* in these olfactory receptors (Fig. S2). Moreover, the behavior tests (T-maze, heavy mineral oil versus ethyl acetate) showed that *DCX-EMAP^{KO}* flies had no obvious olfactory defect (Fig. S2). Therefore, our current data do not support the idea that *DCX-EMAP* also plays a significant role in the olfactory receptor cells.

DCX-EMAP is a structural component of the MOs

We then explored the cellular localization of *DCX-EMAP*. Using *DCX-EMAP^{KI}*, we examined the subcellular localization of *DCX-EMAP* at the endogenous expression level. In haltere receptors, *DCX-EMAP* was primarily observed in the MO and the upper part of the TB (Fig. 3 A). Using the airyscan superresolution microscopy, we were able to resolve that *DCX-EMAP* was located in the central region of the MO in haltere receptors (top view, Fig. 3 B). By referring to the ET image of the MO in haltere receptors (Fig. 1 D), we think that *DCX-EMAP* is most likely localized to the compound cytoskeleton. In leg campaniform and

bristle receptors, *DCX-EMAP* exclusively localized to the MOs (Fig. 3 C). Note that similar localization of *DCX-EMAP* was observed using the transgenic strain (*uas-gfp-DCX-EMAP*; Fig. 3 D), demonstrating that this overexpression strain can also be used to report the subcellular localization. Based on these observations, we conclude that *DCX-EMAP* is mainly located at the MOs.

We next examined whether *DCX-EMAP* is a dynamic or stable component of the MOs. Using fluorescence recovery after photobleaching (FRAP), we found that the signal of *DCX-EMAP* in the MO of leg receptors showed little recovery within 30 min (Fig. 3, E and F). This was similar to that of tubulin (the reference for stable structures) but slower than that of EB1 (the reference for dynamic signals; Fig. 3, E and F; Sun et al., 2021). The relatively lower turnover rate suggests that *DCX-EMAP* is a stable component of the MOs. To further confirm the idea that *DCX-EMAP* is located at the cytoskeleton and forms a stable structure, we studied the location of *DCX-EMAP* in *c01236/BE6* (a *kat-60LI* mutant), where the cytoskeletal structure in the MOs is altered (Sun et al., 2021). In this mutant, *DCX-EMAP* was mislocalized or absent in most of the cells (Fig. 3 G), consistent with the idea. As a control, in *nompC³*, where *NompC* channels are absent but the overall structure of the MOs is fairly normal (Sun et al., 2019), the localization of *DCX-EMAP* was not changed (Fig. 3, H-J). Therefore, we conclude that *DCX-EMAP* is a constitutive component of the compound cytoskeleton in the MOs.

DCX-EMAP is required for the ultrastructure of the MOs but not the TBs

To understand the functional role of *DCX-EMAP*, we analyzed the ultrastructure of the mechanosensory cilia in *DCX-EMAP^{KO}* using 3D EM reconstruction. Serial block-face imaging analysis on haltere receptors showed that the intracellular structure in the MO of *DCX-EMAP^{KO}* was largely disrupted, while that in the TB was normal (Fig. S4 and Video 4). To better characterize the structural changes, we performed ET reconstruction. In haltere receptors, the density of microtubules in the mutant MOs was largely reduced (*wild type*: $240 \pm 50 \mu\text{m}^{-2}$, $n = 3$ cells; *DCX-EMAP^{KO}*: $50 \pm 30 \mu\text{m}^{-2}$, $n = 3$ cells, $P < 0.01$), while that in the TB was not changed (*wild type*: $140 \pm 10 \mu\text{m}^{-2}$, $n = 3$ cells; *DCX-EMAP^{KO}*: $120 \pm 20 \mu\text{m}^{-2}$, $n = 3$ cells, $P = 0.15$; Fig. 4, A and B; and Videos 1, 5, and 6). These results indicate that *DCX-EMAP* promotes the assembly or stability of the MO microtubules. Moreover, we noted that despite the presence of some microtubules in the MOs of *DCX-EMAP^{KO}*, the 3D porous architecture of the EDMs was absent (Fig. 4 A and Videos 1 and 5). The remaining EDMs appeared to be fragmentary (Fig. 4 A), and some were accumulated at the neck region (i.e., the region between the MO and the TB in haltere receptors; Fig. S4). This observation suggests that *DCX-EMAP* is also required for the local organization of the EDMs.

Moreover, we found that the MOs in the haltere receptors of *DCX-EMAP^{KO}* were largely expanded (maximal width, *wild type*: 232 ± 18 nm; *DCX-EMAP^{KO}*: 583 ± 105 nm; $n = 3$ cells, $P < 0.05$; Fig. 4 A). In our previous study, we proposed that the MOs of fly haltere receptors are stretched by lateral tissular tension (Sun et al., 2019), and that this tissular tension tends to expand the

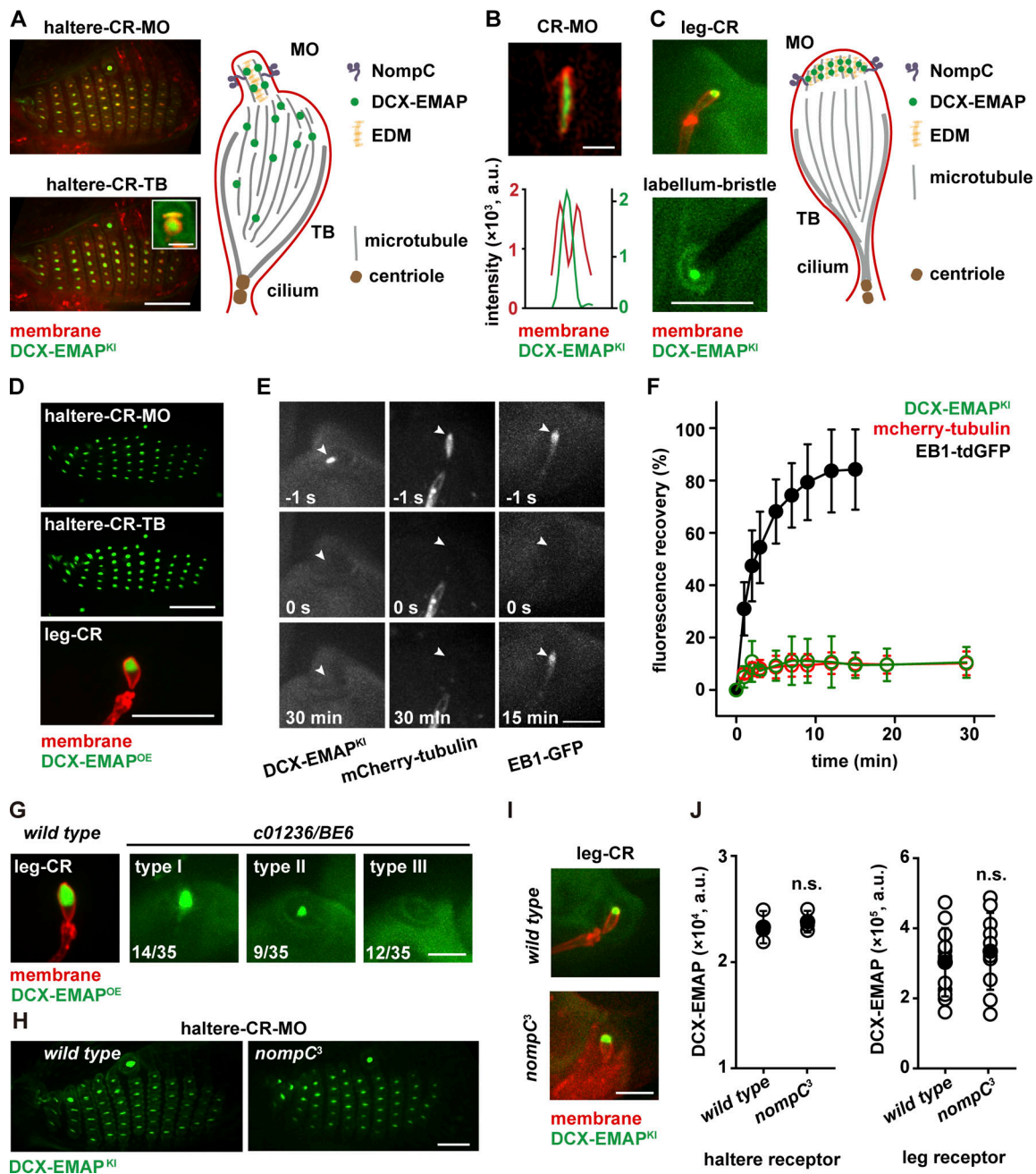


Figure 3. DCX-EMAP is a structural component of the microtubule-based cytoskeleton in the MOs. (A) Endogenous localization of GFP-DCX-EMAP (*DCX-EMAP^{KI}*) in haltere campaniform receptors (top view). Scale bar, 10 μ m. Inset, localization of GFP-DCX-EMAP in the outer segment of a haltere campaniform receptor (lateral view). Inset scale bar, 2 μ m. Genotype: *DCX-EMAP-gal4, uas-cd4-tdtom, and DCX-EMAP^{KI}*. (B) A representative airyscan super-resolution image out of all data from four flies and in total 65 cells (upper) showing the localization of GFP-DCX-EMAP (*DCX-EMAP^{KI}*) at the central region of the MOs (haltere receptor, top view). The corresponding intensity line profiles of the membrane (red) and GFP-DCX-EMAP (green) are shown in the lower panel. Scale bar, 1 μ m. (C) Endogenous localization of GFP-DCX-EMAP (*DCX-EMAP^{KI}*) in leg campaniform (upper panel) and labellum bristle (lower panel) receptors. Genotype: *DCX-EMAP-gal4, uas-cd4-tdtom, DCX-EMAP^{KI}*. Scale bar, 10 μ m. (D) Localization of GFP-DCX-EMAP in haltere (top view) and leg (lateral view) receptors in *DCX-EMAP^{OE}* strain. Genotype: *DCX-EMAP-gal4, uas-cd4-tdtom/uas-gfp-DCX-EMAP*. Scale bar, 10 μ m. (E) Three sets of representative confocal images (lateral view of the leg receptors) showing the recovery of GFP-DCX-EMAP (*DCX-EMAP^{KI}*) signal, mCherry-tubulin (*DCX-EMAP-gal4/uas-mcherry- α Tub84B*), and EB1-GFP (*DCX-EMAP-gal4; uas-Eb1-gfp*). -1 s, right before bleaching. 0 s, just after bleaching. 30 or 15 min, time after bleaching. The white arrowhead in each panel indicates the position of the MO. Scale bar, 5 μ m. (F) Fluorescence recovery curves after photobleaching. Green (open circle), GFP-DCX-EMAP (*DCX-EMAP^{KI}*) recovery in the MOs ($n = 6$ cells). Red (open circle), mCherry-tubulin recovery in the outer segments ($n = 6$ cells). Black (solid circle), EB1-GFP recovery in the outer segments ($n = 12$ cells). Data are presented as mean \pm SEM. (G) Representative images (lateral view) showing the localization of GFP-DCX-EMAP in the leg receptor of wild type (*DCX-EMAP-gal4, uas-cd4-tdtom/uas-gfp-DCX-EMAP*) or the *kat-60L1* mutant (*DCX-EMAP-gal4/uas-gfp-DCX-EMAP; c12306/BE6*). Three types of phenotypes were identified, and the number of cells falling into each type was indicated. Scale bar, 10 μ m. (H and I) Representative images showing the localization of GFP-DCX-EMAP in the haltere (top view; H) and leg receptors (lateral view; I) of wild type (*DCX-EMAP^{KI}/DCX-EMAP-gal4, uas-cd4-tdtom*) or the *nompC* null mutant (*nompC³; DCX-EMAP^{KI}/DCX-EMAP-gal4, uas-cd4-tdtom*). Scale bar, 5 μ m. (J) Statistical quantification of DCX-EMAP signal in the MOs of haltere ($n = 3$ halteres for wild type and *nompC³*, respectively) and leg receptors (wild type: $n = 12$ cells; *nompC³*: $n = 10$ cells). Data are presented as mean \pm SD with scattered data points. Two-sided unpaired Student's *t* test. n.s., no significance.

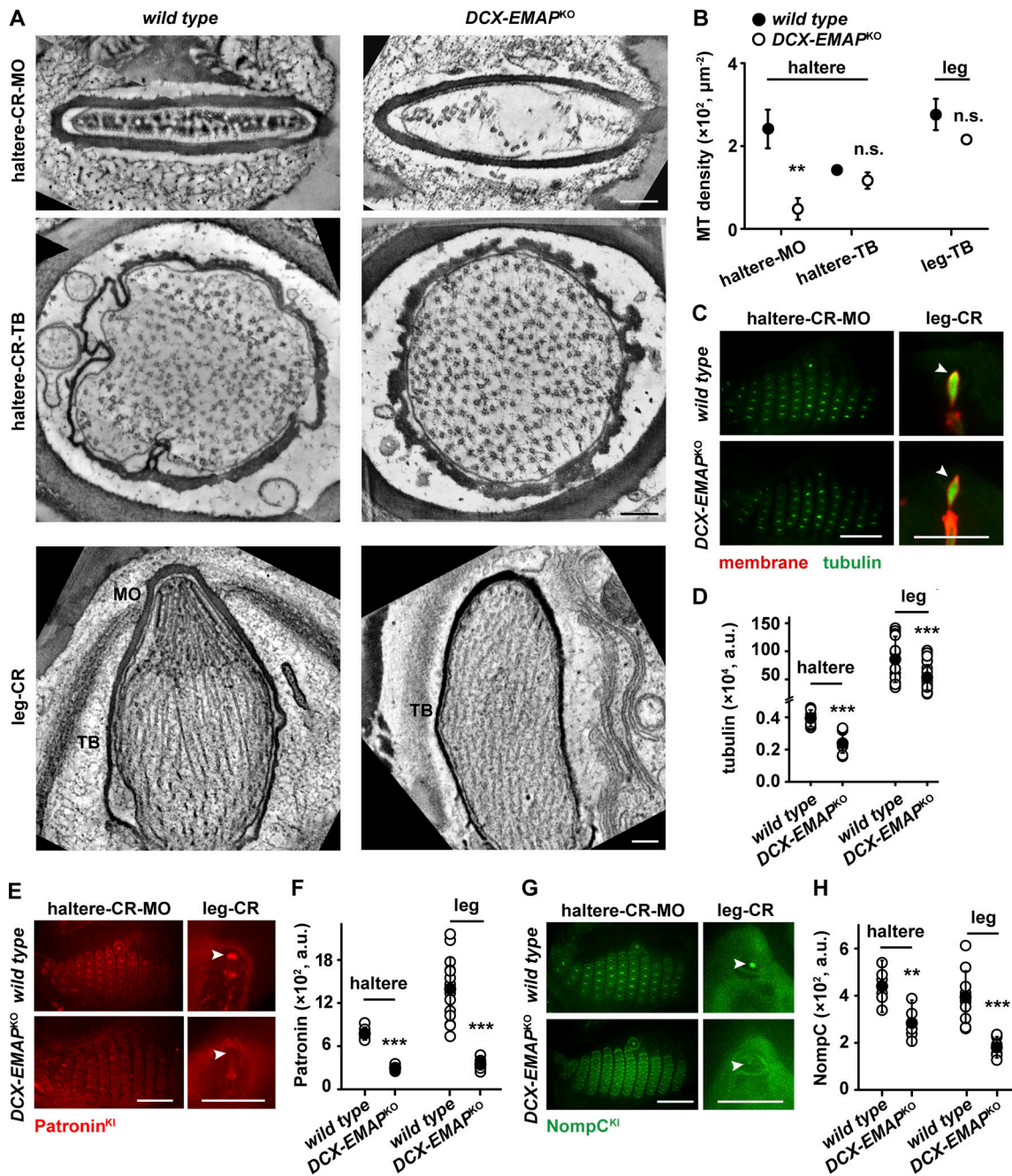


Figure 4. DCX-EMAP is required for the ultrastructure of the MOs but not the TBs. (A) Representative ET slices images of the outer segment of haltere and leg receptors in *wild type* (left panels) and *DCX-EMAP^{KO}* (right panels). Scale bar, 200 nm. Also see Videos 1, 2, 5, and 7. (B) Statistical quantification of microtubule density in the MO and TB of haltere and leg receptors in *wild type* ($n = 3$ cells) and *DCX-EMAP^{KO}* ($n = 3$ cells). (C) Representative confocal images showing GFP-tubulin signal in the haltere (top view) and leg receptors (lateral view) in *wild type* (*DCX-EMAP-gal4, uas-cd4-tdtom/uas-gfp- α Tub84B*) and *DCX-EMAP^{KO}* (*DCX-EMAP-gal4, uas-cd4-tdtom/uas-gfp- α Tub84B; DCX-EMAP^{KO}*). The white arrowhead indicated the distal region of the outer segment in the leg receptors. Scale bar, 10 μm . (D) Statistical quantification of GFP-tubulin signal in the MOs of haltere receptors (*wild type*: $n = 9$ halteres; *DCX-EMAP^{KO}*: $n = 9$ halteres) and in the entire outer segment of leg receptors (*wild type*: $n = 17$ cells; *DCX-EMAP^{KO}*: $n = 25$ cells). (E) Representative confocal images showing Patronin-RFP signal in the haltere (top view) and leg receptors (lateral view) of *wild type* (*Patronin-RFP^{Kl}*) and *DCX-EMAP^{KO}* (*Patronin-RFP^{Kl}; DCX-EMAP^{KO}*). The white arrowheads indicate the position of the MOs. Scale bar, 10 μm . (F) Statistical quantification of Patronin-RFP signal in the MOs of haltere (*wild type*: $n = 6$ halteres; *DCX-EMAP^{KO}*: $n = 6$ halteres) and leg receptors (*wild type*: $n = 14$ cells; *DCX-EMAP^{KO}*: $n = 8$ cells). (G) Representative confocal images showing NompC-GFP signal in the haltere (top view) and leg receptors (lateral view) in *wild type* (*nompC-GFP^{Kl}*) and *DCX-EMAP^{KO}* (*nompC-GFP^{Kl}; DCX-EMAP^{KO}*). The white arrowheads indicate the MO region. Scale bar, 10 μm . (H) Statistical quantification of NompC-GFP signal in the MOs of haltere (*wild type*: $n = 6$ halteres; *DCX-EMAP^{KO}*: $n = 6$ halteres) and leg receptors (*wild type*: $n = 10$ cells; *DCX-EMAP^{KO}*: $n = 6$ cells). In panels B, D, F, and H, data are presented as mean \pm SD with scattered data points. Two-sided unpaired Student's *t* test. **, $P < 0.01$; ***, $P < 0.001$; n.s., no significance.

MOs. In wild-type cells, this tissular tension is balanced by a force on the membrane-microtubule connectors (MMCs). In this model, the compound cytoskeleton, located in the middle of the MO, acts as a mechanical hub by holding all MMCs. A prediction of this model is if this hub is absent, the MOs would be expanded due to the loss of the counteracting forces. This is consistent with our observation in *DCX-EMAP^{KO}* and suggests that DCX-EMAP also plays a mechanical role in the MOs.

In the leg receptors of *DCX-EMAP^{KO}*, the MO (i.e., the region with the EDMs) disappeared (Fig. 4 A). The microtubules in the TB had a similar density to those in wild-type cells (*wild type*: $270 \pm 40 \mu\text{m}^{-2}$, $n = 3$ cells; *DCX-EMAP^{KO}*: $220 \pm 10 \mu\text{m}^{-2}$, $n = 3$ cells, $P = 0.10$; Fig. 4 B) and filled in the distal region of the outer segment (Fig. 4 A and Video 7). Some isolated EDM aggregates were associated with the tip region of the microtubules, but no organized EDM structure was observed (Fig. 4 A and Video 7), similar to the observation in haltere receptors.

We further examined the molecular organization of the MOs by examining the localization of several known markers using light microscopy. In haltere receptors, the tubulin signal in the distal region of the outer segment was reduced in *DCX-EMAP^{KO}* (Fig. 4, C and D), consistent with the loss of microtubules in the MOs. In leg receptors, the distal region in the outer segment of *DCX-EMAP^{KO}* became smaller than that in wild type, and the tubulin signal was weaker (Fig. 4, C and D), consistent with the absence of the MO region observed in our ET data (Fig. 4 A). In addition, we previously established that the proximal ends of the MO microtubules are marked by Patronin (Sun et al., 2021). In the mutant receptors, the Patronin signal was absent in both haltere and leg receptors (Fig. 4, E and F), consistent with the loss of short microtubules in the MOs. Finally, we found that despite having a correct localization, NompC showed a reduced signal in both types of receptors (Fig. 4, G and H). In all, these observations suggest that DCX-EMAP is key for the molecular organization of the MOs.

The doublecortin tandem stabilizes microtubules by reducing k_{off} of tubulin dimers at both growing and shrinking microtubule ends

Having characterized the structural and molecular phenotypes in *DCX-EMAP^{KO}*, we explored how DCX-EMAP works at the molecular level. We first determined the microtubule-binding/stabilizing domain of DCX-EMAP. The DCX domain of DCX-EMAP had only a 33% sequence identity to human DCX but a similar structure (Fig. S5), suggesting a high level of structural homology. Ectopic expression of full-length DCX-EMAP, $\Delta\text{DCX1/2}$ (DCX domain deletion), or DCX1/2 (all tagged with GFP) in S2 cells showed that the DCX tandem was necessary and sufficient for the microtubule-binding activity (Fig. 5, A and B). We then analyzed how the DCX1/2 domain regulates the properties of microtubules using the in vitro microtubule dynamics assay. Note that in the present study, we used tubulin purified from fly S2 cells instead of porcine brain tubulin, so the major protein reactants in the system were both of fly origin (Fig. S5). We noted that the growth of fly S2 tubulin could be observed at a relatively low tubulin concentration, around $2 \mu\text{M}$ (Fig. 5, C and D), suggesting a higher polymerization affinity in comparison

with the conventionally used porcine or bovine brain tubulin. We found that DCX1/2 ($0.5 \mu\text{M}$) further reduced the critical concentration of fly S2 tubulin in polymerization ($C_{0-\text{fly}}$: $1.1 \mu\text{M}$; $C_{0-\text{DCX1/2}}$: $0.4 \mu\text{M}$; 28°C , Fig. 5 D). Moreover, it had a moderate effect on the growth rate but a largely reduced catastrophe frequency of dynamic microtubules (Fig. 5, D and E). Kinetics analysis showed that DCX1/2 primarily reduced the off-rate and had a mild effect on the on-rate of tubulin dimers at growing microtubule ends ($k_{\text{on}} = 3.7 \text{ dimers} \cdot \mu\text{M}^{-1} \cdot \text{s}^{-1}$, $k_{\text{on-DCX1/2}} = 3.1 \text{ dimers} \cdot \mu\text{M}^{-1} \cdot \text{s}^{-1}$; $k_{\text{off}} = 4.0 \text{ dimers} \cdot \text{s}^{-1}$, $k_{\text{off-DCX1/2}} = 1.1 \text{ dimers} \cdot \text{s}^{-1}$; Fig. 5 D). Based on the previously proposed models for microtubule polymerization and catastrophe (Bowne-Anderson et al., 2015; Howard, 2001), our results showed that the reduced off-rate is the major factor that accounts for the lower critical concentration, increased growth rate, and lower catastrophe frequency. Moreover, DCX1/2 significantly reduced the depolymerization rate of microtubules in the shrinking phase, suggesting that the off-rate of tubulin dimers at shrinking microtubule ends is also reduced (Fig. 5 F). Therefore, we conclude that DCX1/2 stabilizes microtubules by reducing the off-rate of tubulin dimers from both growing and shrinking microtubule ends.

The complete doublecortin tandem is required for the microtubule-stabilizing activity

Inspired by a recent work on the differential roles of two doublecortin domains in human DCX (Manka and Moores, 2020), we evaluated the functions of the pseudo-repeats in the DCX domain of DCX-EMAP. Similar to the observations for human DCX, the binding affinity of DCX1 on dynamic microtubules was significantly lower than that of the DCX tandem and the binding affinity of DCX2 was even lower (Fig. 5, G and H). Meanwhile, we found that the DCX tandem showed a distinct affinity for different tubulin states. For example, both DCX1/2 and DCX1 domains showed more binding to dynamic microtubules (GDP) than to the GMPCPP (a slowly hydrolyzable analog of GTP) seeds (Fig. 5, G and H). On the contrary, the DCX2 domain preferentially bound to GMPCPP microtubules (Fig. 5, G and H). These results are consistent with the previous report that the CDC of human DCX preferentially binds to the rapidly assembled microtubules (analog of GTP microtubules), thereby supporting the differential roles of the CDC and NDC in the function of DCX (Manka and Moores, 2020). In agreement with the binding experiments, adding $0.5 \mu\text{M}$ DCX1 or DCX2 or DCX1+DCX2 mixture ($0.5 \mu\text{M}$ for each) had no significant effect on microtubule dynamics (tubulin = $2 \mu\text{M}$; Fig. 5, I-K). Therefore, both DCX domains and the structural linkage between them are required for the intact microtubule-binding/stabilizing activity of DCX-EMAP.

The TAPE domain is unlikely to play a major role in the microtubule-binding activity of DCX-EMAP

We then explored the biochemical function of the TAPE domain in vitro. First, we tested if DCX-EMAP could form oligomers via the TAPE domain. When the $\Delta\text{DCX1/2}$ mutant (i.e., the TAPE domain) and full-length DCX-EMAP were co-expressed, no co-localization was observed, suggesting that the TAPE domain has

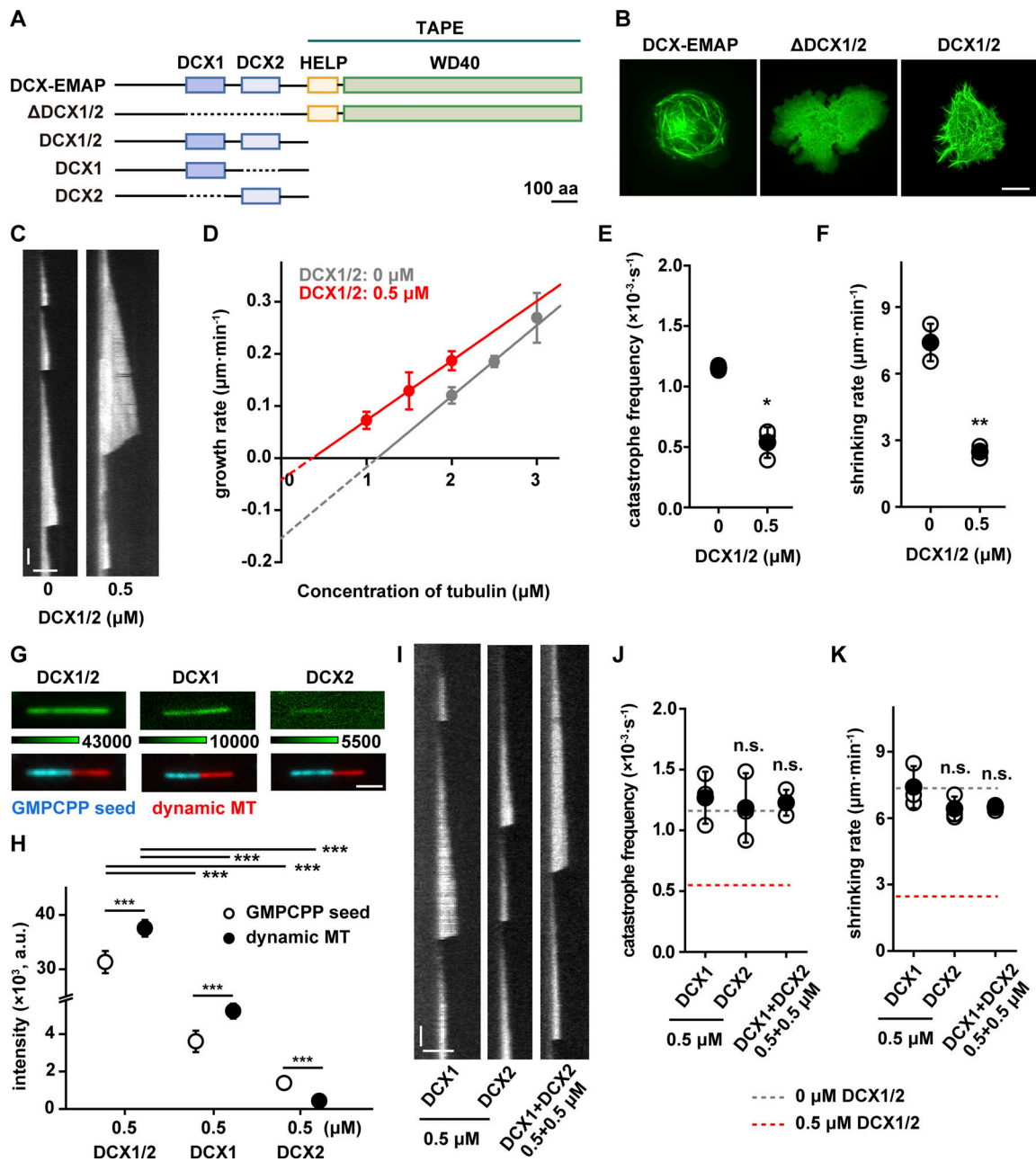


Figure 5. DCX-EMAP stabilizes microtubule by reducing k_{off} of tubulin dimers from both growing and shrinking microtubule ends. (A) Schematic diagrams of various DCX-EMAP mutants. (B) Representative confocal images showing the microtubule-binding ability of full-length DCX-EMAP, Δ DCX1/2, and DCX1/2 in S2 cells. Scale bar, 10 μ m. (C) Representative kymographs of microtubule dynamics (tubulin: 2 μ M) in the presence 0 or 0.5 μ M DCX1/2. Vertical bar, 1 min. Horizontal bar, 2 μ m. (D) Plots of the microtubule plus end growth rate as a function of tubulin concentration in the presence of 0 (gray; $n = 182, 212,$ and 202 events from three assays) or 0.5 μ M (red; $n = 138, 109, 135$ events from three assays) DCX1/2. (E) Statistical quantification of microtubule catastrophe frequency (tubulin: 2 μ M) in the presence 0 ($n = 97$ microtubules from three assays) or 0.5 μ M ($n = 87$ microtubules from three assays) DCX1/2. (F) Statistical quantification of microtubule shrinking rate (tubulin: 2 μ M) in the presence of 0 ($n = 94$ events from three assays) or 0.5 μ M ($n = 46$ events from three assays) DCX1/2. (G) Representative TIRF images showing the binding of DCX1/2, DCX1, or DCX2 (0.5 μ M) to the GMPCPP-stabilized (blue) and dynamic (red) microtubules. Scale bar, 2 μ m. (H) Statistical quantification of the binding of DCX1/2, DCX1, or DCX2 (0.5 μ M) on GMPCPP-stabilized and dynamic microtubules ($n = 90$ microtubules from three assays). (I) Representative kymographs of microtubule dynamics (tubulin: 2 μ M) in the presence of DCX1 (0.5 μ M), DCX2 (0.5 μ M), or DCX1+DCX2 mixture (0.5 μ M each). Vertical bar, 1 min; horizontal bar, 2 μ m. (J) Statistical quantification of microtubule catastrophe frequency in the presence of DCX1 (0.5 μ M, $n = 95$ microtubules from three assays), DCX2 (0.5 μ M, $n = 94$ microtubules from three assays), or DCX1+DCX2 mixture (0.5 μ M each, $n = 67$ microtubules from three assays). (K) Statistical quantification of microtubule shrinking rate in the presence of DCX1 (0.5 μ M, $n = 83$ events from three assays), DCX2 (0.5 μ M, $n = 89$ events from three assays), or DCX1+DCX2 mixture (0.5 μ M each, $n = 89$ events from three assays). Data are presented as mean \pm SD with scattered data points. Two-sided unpaired Student's t test. *, $P < 0.05$. **, $P < 0.01$. ***, $P < 0.001$. n.s., no significance.

no self-interaction (Fig. S5). Second, we examined if the TAPE domain directly binds to microtubules. When mCherry- Δ DCX1/2 (i.e., mCherry-TAPE) was expressed in S2 cells (Fig. S5), no microtubule-associated signal was observed. A recent study showed that either the carboxyl- or amino-terminal fusion protein may interfere with the microtubule-binding activity of the TAPE domain of EML2-S (TAPE_{EML2-S}; Hotta et al., 2022). To rule out this possibility, we tagged the TAPE domain using the HA tag, which has a smaller size, and observed its localization using immunofluorescence. In this experiment, we still did not observe any microtubule-associated signal (Fig. S5). Therefore, we conclude that the microtubule-binding affinity of the TAPE domain should be at least significantly weaker than that of the DCX tandem in DCX-EMAP. Note that the observations in the S2 cell cannot absolutely rule out the microtubule-binding affinity of the TAPE domain.

The TAPE domain of other EMAP proteins, including TAPE_{EML2-S}, showed a clear microtubule-associated signal (Hotta et al., 2022). We wondered why the TAPE domain of DCX-EMAP showed no microtubule-associated signal in cells. It was shown that TAPE_{EML2-S} binds to microtubules using a combination of electrostatic and hydrophobic interactions. These interactions require a cluster of four basic residues (i.e., the R-patch) and a group of three hydrophobic residues at the amino-terminal of the β -propeller in TAPE_{EML2-S}. Sequence analysis revealed that in DCX-EMAP, the R-patch was conserved, but two of the three residues that form the hydrophobic interface were substituted with the hydrophilic ones (e.g., H672 and T674; Fig. S5). The third hydrophobic residue (L627) remained, but the structure model predicted using the AlphaFold database showed that its side chain was facing in the opposite direction (Fig. S5). Therefore, the hydrophobic interface required for the microtubule-binding activity did not exist in the TAPE domain of DCX-EMAP. This analysis provides a structural basis to understand the difference in the microtubule-associated behavior of different TAPE domains.

In all, based on these observations and analysis, we think that the TAPE domain of DCX-EMAP is unlikely to play a major role in the microtubule binding behavior of DCX-EMAP, and its function needs to be further analyzed in vivo.

DCX-EMAP has dual roles in the formation of the MOs

We then studied the working mechanism of DCX-EMAP by analyzing the functional roles of its domains in vivo. First, because the DCX domain likely dominates the microtubule-binding/stabilizing activity of DCX-EMAP, we analyzed its roles in vivo. To this end, we generated three transgenic lines: (1) DCX-EMAP ^{Δ DCX1/2}; (2) DCX-EMAP ^{Δ DCX1}; and (3) DCX-EMAP ^{Δ DCX2} (Fig. 6 A). When crossed to the DCX-EMAP-*gal4* driver line, lines 1 and 3 were able to express the GFP-tagged DCX-EMAP mutant proteins. However, no visible GFP-tagged protein could be detected when line 2 was used (Fig. 6 A). We suspect that the mutant protein (i.e., Δ DCX1), expected to be expressed in line 2, is probably unstable and subjected to degradation pathways in vivo. When crossed to the DCX-EMAP^{KO} or wild-type strain, both Δ DCX1/2 and Δ DCX2 were able to specifically localize to the distal tip of the outer segment, with no obvious signal detected

in the proximal part (i.e., the TB; Fig. 6, A–E). Moreover, ET analysis showed that the structure of the MO region was not recovered in DCX-EMAP ^{Δ DCX1/2}. In particular, the observation of fragmentary EDMs (Fig. 6, F and G; and Video 8) suggests that the TAPE domain is not sufficient to organize the porous structure of the EDMs and that the intact microtubule-binding/stabilizing activity of DCX-EMAP is required.

Second, the observations in DCX-EMAP ^{Δ DCX1/2} suggest that the TAPE domain contributes to the MO-specific localization of DCX-EMAP. Because the TAPE domain consists of the HELP and WD40 domains, we generated two additional lines (DCX-EMAP ^{Δ HELP} and DCX-EMAP ^{Δ WD40}) to further refine their functional roles (Fig. 6 A). We found that no matter whether it was expressed in the DCX-EMAP^{KO} or wild-type background, Δ HELP showed a homogeneous distribution throughout the entire outer segment and also appeared in the dendritic inner segment (Fig. 6, A–E), namely that it lost the MO-specific localization. On the contrary, Δ WD40 still showed a localization preference to the distal region of the MOs, but note that this preference was more prominent in the wild type than in the DCX-EMAP^{KO} background (Fig. 6, A–E). In all, these observations suggest that the HELP domain is key for the MO localization of DCX-EMAP and the normal structure of the MO could facilitate its localizing role.

Third, when expressed in the DCX-EMAP^{KO} background, DCX-EMAP ^{Δ WD40} is expected to encode a mutant protein with the intact DCX domain and the HELP domain. We noted that Δ WD40 could still localize to the MO and the amount of Δ WD40 in the MO region was comparable with that in the DCX-EMAP^{KI} strain (Fig. 6 C). However, ET analysis showed that like in DCX-EMAP^{KO}, the MO region was not restored by Δ WD40, and the EDMs were still fragmentary (Fig. 6, F and G; and Video 9). Therefore, the WD40 domain is required to organize the 3D structure of the EDMs.

Finally, to evaluate the functional rescue of DCX-EMAP ^{Δ DCX1/2}, DCX-EMAP ^{Δ DCX2}, DCX-EMAP ^{Δ HELP}, and DCX-EMAP ^{Δ WD40}, we performed the crawling behavioral test. Consistent with the cellular observations, none of these strains could rescue the behavioral phenotypes observed in DCX-EMAP^{KO} (Fig. 6 H and Video 10). Therefore, DCX-EMAP is a key factor in the formation of the MOs by stabilizing and organizing the “microtubule-EDM” complex in the compound cytoskeleton in the MOs.

The localization of DCX-EMAP is achieved via a two-step process

Having established the functions of DCX-EMAP, we then explored how the MO-specific localization of DCX-EMAP is achieved. Because the MOs are structurally integrated with extracellular sheath (Fig. 1 H), we first considered if the extracellular factors help to organize the structure of the MO and in turn determine the localization of the mechanosensory molecules (e.g., NompC or DCX-EMAP). To address this issue, we checked the endogenous localization of NompC and DCX-EMAP in the *nompA* null mutant (*nompA*^{1/2}), where the physical contact between the MO and sheath is lost (Chung et al., 2001). In *nompA*^{1/2}, the signal of NompC was not limited to the MOs,

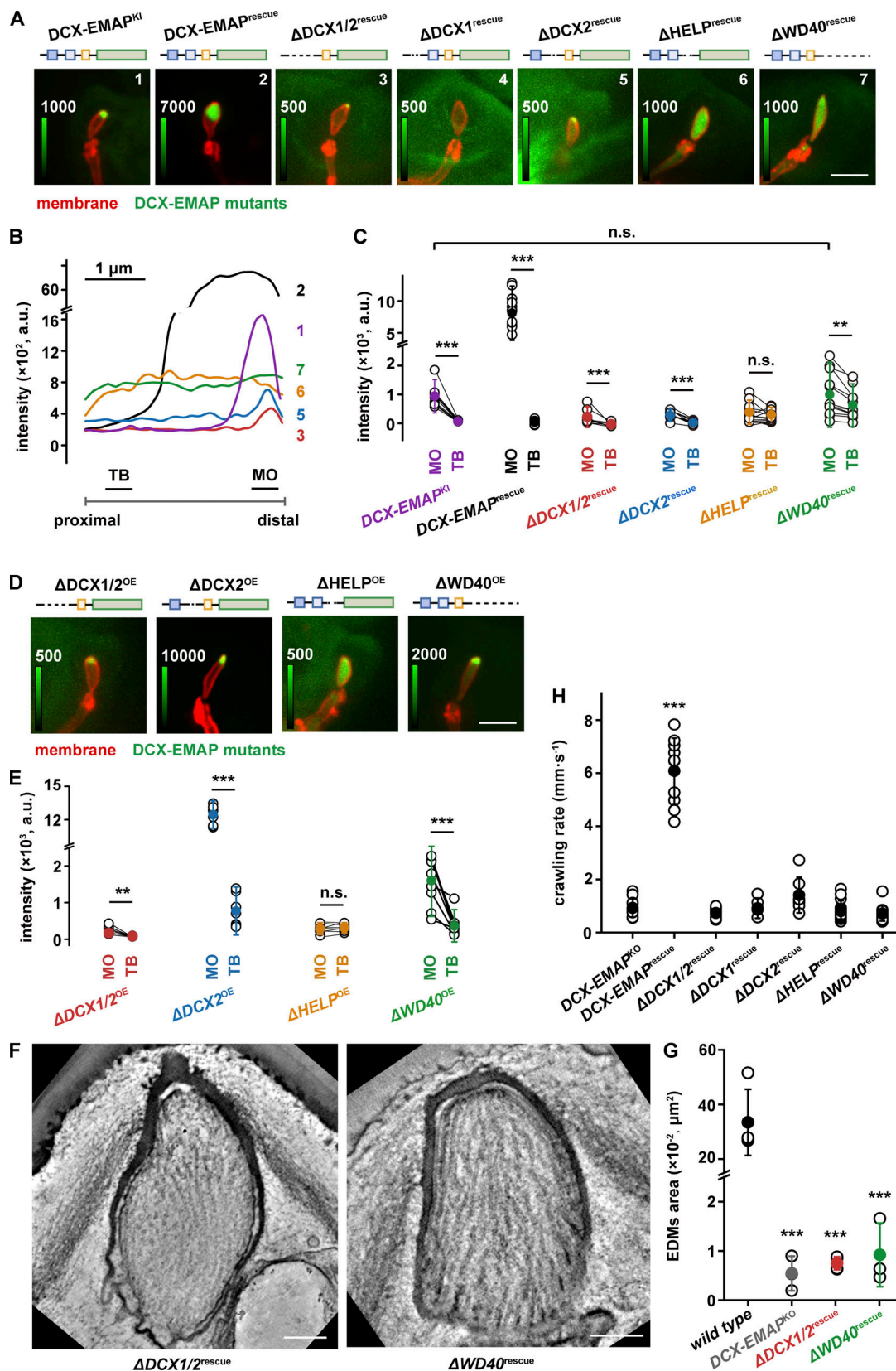


Figure 6. **DCX-EMAP organizes the ultrastructure of the MO.** (A) Representative confocal images (lateral view of leg receptors) showing the localization of DCX-EMAP and its various mutants as indicated. Scale bar, 5 μm. Genotypes: 1. *DCX-EMAP-gal4,uas-cd4-tdtom/+; DCX-EMAP^{KI}*. 2. *DCX-EMAP-gal4,uas-cd4-tdtom/uas-gfp-DCX-EMAP; DCX-EMAP^{KO}*. 3. *DCX-EMAP-gal4,uas-cd4-tdtom/uas-gfp-ΔDCX1/2; DCX-EMAP^{KO}*. 4. *DCX-EMAP-gal4,uas-cd4-tdtom/uas-gfp-ΔDCX1; DCX-EMAP^{KO}*. 5. *DCX-EMAP-gal4,uas-cd4-tdtom/uas-gfp-ΔDCX2; DCX-EMAP^{KO}*. 6. *DCX-EMAP-gal4,uas-cd4-tdtom/uas-gfp-ΔHELP; DCX-EMAP^{KO}*. 7. *DCX-EMAP-gal4,uas-cd4-tdtom/uas-gfp-ΔWD40; DCX-EMAP^{KO}*. (B) Line graph showing the intensity profile of DCX-EMAP and its mutants along the proximal-distal axis of the leg receptor. (C) Dot plot showing the intensity of DCX-EMAP and its mutants at the MO and TB. (D) Confocal images showing the localization of DCX-EMAP overexpression mutants. (E) Dot plot showing the intensity of DCX-EMAP overexpression mutants at the MO and TB. (F) Electron micrographs showing the ultrastructure of the MO in *ΔDCX1/2^{rescue}* and *ΔWD40^{rescue}* genotypes. (G) Dot plot showing the area of electron-dense microtubule bundles (EDMs) in wild type and mutant genotypes.

gal4, uas-cd4-tdtom/uas-gfp-ΔWD40; *DCX-EMAP^{KO}*. **(B)** Representative intensity line profiles of GFP-DCX-EMAP and its various mutants along the distal-proximal axis of the outer segment in the leg receptors (*DCX-EMAP^{KO}* background). Two short bars indicate the regions where the fluorescence signals for the TB and MO were measured. **(C)** Statistical quantification of the intensity of GFP-DCX-EMAP and the mutants (*n* = 9, 13, 9, 9, 15, and 12 cells) in the MO and TB of the leg receptors. **(D)** Representative confocal images (lateral view of leg receptors) showing the localization of four *DCX-EMAP* mutants (*wild type* background). Scale bar, 5 μm. Genotypes: 1. *DCX-EMAP-gal4, uas-cd4-tdtom/uas-gfp-ΔDCX1/2*. 2. *DCX-EMAP-gal4, uas-cd4-tdtom/uas-gfp-ΔWD40*. 3. *DCX-EMAP-gal4, uas-cd4-tdtom/uas-gfp-ΔHELP*. 4. *DCX-EMAP-gal4, uas-cd4-tdtom/uas-gfp-ΔWD40*. **(E)** Statistical quantification of the intensity of GFP-DCX-EMAP and its mutants shown in D (*n* = 7, 7, 8, and 9 cells) in the MO and TB of the leg receptors. **(F)** Representative ET slices images of leg receptors (lateral view) in *ΔDCX1/2^{rescue}* (left panel) and *ΔWD40^{rescue}* (right panel). Scale bar, 300 nm. Also see Videos 8 and 9. **(G)** Statistics quantification of the area of the EDMs observed in the ET slice images of the leg receptors in *wild type* (*n* = 4 cells), *DCX-EMAP^{KO}* (*n* = 3 cells), *ΔDCX1/2^{rescue}* (*n* = 4 cells) and *ΔWD40^{rescue}* (*n* = 3 cells). **(H)** Crawling tests of *DCX-EMAP^{KO}* (*n* = 11 flies), *DCX-EMAP^{rescue}* (*DCX-EMAP-gal4/uas-gfp-DCX-EMAP*; *DCX-EMAP^{KO}*, *n* = 10 flies), *ΔDCX1/2^{rescue}* (*DCX-EMAP-gal4/uas-gfp-ΔDCX1/2*; *DCX-EMAP^{KO}*, *n* = 15 flies), *ΔDCX1^{rescue}* (*DCX-EMAP-gal4/uas-gfp-ΔDCX1*; *DCX-EMAP^{KO}*, *n* = 5 flies), *ΔDCX2^{rescue}* (*DCX-EMAP-gal4/uas-gfp-ΔDCX2*; *DCX-EMAP^{KO}*, *n* = 15 flies), *ΔHELP^{rescue}* (*DCX-EMAP-gal4/uas-gfp-ΔHELP*; *DCX-EMAP^{KO}*, *n* = 15 flies), and *ΔWD40^{rescue}* (*DCX-EMAP-gal4/uas-gfp-ΔWD40*; *DCX-EMAP^{KO}*, *n* = 14 flies). Also see Video 10. In C, E, G, and H, data are presented as mean ± SD with scattered data points. In C and E, for comparison between different strains, two-sided unpaired Student's *t* test was used. For comparison between TB and MO from the same cell, two-sided paired Student's *t* test was used. **, *P* < 0.01; ***, *P* < 0.001; n.s., no significance.

but diffused to the membrane of the entire outer segment (Fig. 7 A), suggesting that the extracellular contact contributes to the localization of NompC channels. On the contrary, DCX-EMAP still showed a MO-specific localization (Fig. 7 A), suggesting that it is primarily located by intracellular mechanisms and the extracellular contact is largely dispensable. These observations suggest that although the MO can be considered as a structural-mechanical entity, the localizations of its components (such as NompC and DCX-EMAP) can be regulated by different mechanisms.

To further understand how DCX-EMAP is located to and inside the sensory cilium, we first studied the localization of DCX-EMAP in a mutant in which the expression of *Klp64D*, which encodes a subunit of fly kinesin-II (i.e., the anterograde motor

for intraflagellar transport [IFT]), was knocked down (*Klp64Dⁱ*). In all *Klp64Dⁱ* cells, the mechanosensory cilia could still be observed but all had distorted morphologies (Fig. 7 B), suggesting that the ciliary structures are largely disrupted. Close inspection revealed two types of phenotypes. First, in some leg receptor cells of *Klp64Dⁱ* (type I: 7 in 15 cells), DCX-EMAP was enriched in the distal end of the dendritic inner segment (i.e., a region around the basal body) and nothing was observed in the outer segment (Fig. 7 B), suggesting that the IFT mechanism is required for the ciliary entry of DCX-EMAP. To understand whether the accumulation of DCX-EMAP at the dendritic inner segment relies on the basal body, we studied a mutant of *DSas-4* (*DSas-4^{S2214}*), in which the centriole and the entire sensory cilia are absent (Basto et al., 2006). In *DSas-4^{S2214}*, the accumulation

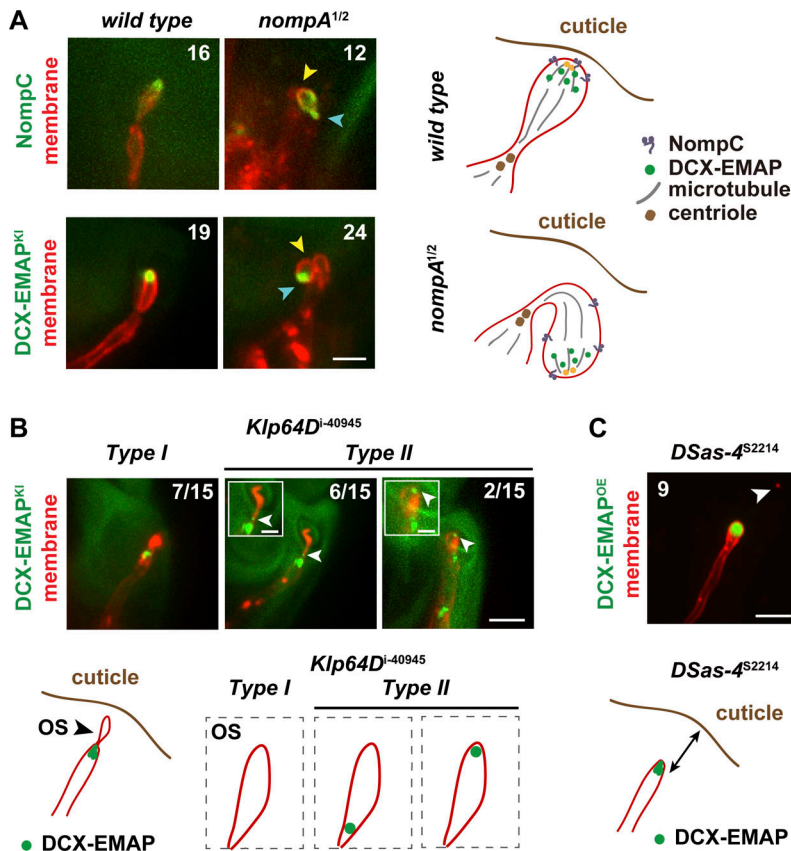


Figure 7. The localization of DCX-EMAP is achieved via a two-step process. **(A)** Representative confocal images showing the localization of NompC and DCX-EMAP in *wild type* and *nompA^{1/2}*. The blue and yellow arrowheads indicate the distal and proximal ends of the outer segment, respectively. The number of cells observed for each genotype is indicated. Scale bar, 5 μm. The cartoon schematics showing the localization of NompC and DCX-EMAP in the outer segment of *wild type* and *nompA^{1/2}* are shown in the right panel. Genotypes: *DCX-EMAP-gal4, uas-cd4-tdtom/uas-nompC-gfp, nompA^{1/2}/nompA^{1/2}*; *DCX-EMAP-gal4, uas-cd4-tdtom/uas-nompC-gfp, DCX-EMAP-gal4, uas-cd4-tdtom/DCX-EMAP^{K1}, nompA^{1/2}/nompA^{1/2}*; *DCX-EMAP-gal4, uas-cd4-tdtom/DCX-EMAP^{K1}*. **(B)** Upper panel: Representative confocal images showing two types of localizations of GFP-DCX-EMAP in *Klp64Dⁱ⁻⁴⁰⁹⁴⁵* (*DCX-EMAP-gal4, uas-cd4-tdtom/Klp64Dⁱ⁻⁴⁰⁹⁴⁵*; *DCX-EMAP^{K1}*). The white arrowhead in the images of the type II localization indicates a DCX-EMAP signal within the outer segment. The number of cells falling into each type of localization is indicated. Scale bar, 5 μm. Inset scale bar, 2 μm. Lower panel: Cartoon schematics showing the corresponding localization of GFP-DCX-EMAP in *Klp64Dⁱ⁻⁴⁰⁹⁴⁵*. The black arrowhead indicates the outer segment. **(C)** Upper panel: Representative confocal images showing the localization of DCX-EMAP in *DSas-4^{S2214}* (*DCX-EMAP-gal4, uas-cd4-tdtom/uas-gfp-DCX-EMAP*; *DSas-4^{S2214}*). The white arrowhead indicates the distalmost tip of the leg receptor, where the dome-like cuticle structure was. Scale bar, 5 μm. Lower panel: Cartoon schematics showing the localization of DCX-EMAP in *DSas-4^{S2214}*. The two-sided arrow indicates the gap between the dendritic tip to the dome-like cuticle structure of the leg receptor.

of DCX-EMAP at the distal tip of the dendrite could still be observed (Fig. 7 C), suggesting that the dendritic mechanism that delivers or gathers DCX-EMAP to the distal end of the inner segment is independent on the basal body. Second, in the other cells of *Klp64Dⁱ* (type II: 8 in 15 cells), a small amount of DCX-EMAP signals could be observed inside the outer segment. Some of the DCX-EMAP signals failed to reach the distal region and appeared at the proximal end of the TB (Fig. 7 B), suggesting that kinesin-II also contributes to the MO-specific localization inside the sensory cilia. Based on these observations, we propose that DCX-EMAP is localized to the MOs through a two-step process, in which a dendritic mechanism first collects DCX-EMAP to the distal region of the dendrite and then the ciliary trafficking mechanism (e.g., IFT) further delivers it into the cilium and finally to the MOs.

Discussion

In the present study, we resolve the 3D ultrastructural organization of the compound cytoskeleton in fly MOs. By studying the function and working mechanism of DCX-EMAP, we provide novel insights into understanding how fly MOs are formed. The key finding is that DCX-EMAP, an essential molecule for fly mechanotransduction, serves as the core ultrastructural organizer of the MOs by locally stabilizing and organizing the microtubule-EDM complex. We now discuss the main conclusions and their implications.

Cellular roles of DCX-EMAP in the formation of fly MOs

Our results demonstrate that the DCX tandem and the TAPE domain (i.e., the HELP + WD40 domains) are all required for the *in vivo* function of DCX-EMAP (Fig. 8 A). First, *in vitro* analysis shows that the DCX tandem of DCX-EMAP has a microtubule-binding/stabilizing activity, in which both DCX domains and the structural linkage in between are required (Fig. 5). *In vivo* experiments show that the mutant DCX-EMAP with no or only one DCX domain cannot rescue the cellular and functional phenotypes of *DCX-EMAP^{KO}* (Fig. 6), suggesting that the intact microtubule-binding/stabilizing activity is required for the formation of the MOs (Fig. 8 A). Second, the HELP domain is conserved among all EMAP family members (Bechstetd et al., 2010). We show that the HELP domain of DCX-EMAP is key for the MO-specific localization (Fig. 6 and Fig. 8 A). However, it is not yet clear how the HELP works at the molecular level. We speculate that it might interact with other components of the MOs (such as the EDMs) or ciliary motors that are responsible for the directional transport to the MOs. Third, the WD40 domain, a known molecular platform to mediate protein-protein interactions, is also conserved in the EMAP family. In the present study, we noted that Δ WD40 could still localize to the MO but the 3D porous structure of the EDMs is absent, suggesting that the WD40 domain of DCX-EMAP is key for the local organization of the EDMs (Fig. 8 A). To refine the *in vivo* working mechanism of the HELP and WD40 domains in this model, it would be essential to identify more components of the EDMs in future studies.

Based on these findings, we propose that DCX-EMAP serves as a component in the structural link between the microtubules and EDMs in the MOs. More specifically, the DCX tandem promotes the assembly and stabilization of short microtubules in the MOs (Fig. 8, B and C). The HELP and WD40 domains mediate the localization signal and organize the EDMs. In this model, DCX-EMAP promotes the assembly and stability of the MO microtubules, which would facilitate local accumulation of the EDMs and DCX-EMAP by providing more landing or binding sites. Then, an increase in the amount of DCX-EMAP would in turn promote the assembly or stability of more MO microtubules, thereby mediating a positive feedback loop (Fig. 8, B and C).

In the previous study, we showed that short microtubules, generated by the “kat-60LI-patronin” module, provide conformational flexibility in the formation of the compound cytoskeleton within the nanoscopic space of the MOs. As a concurrent mechanism, the positive feedback loop mediated by DCX-EMAP would facilitate the full assembly of all other components into a compound cytoskeleton in the MOs (Fig. 8, B and C). The sensillar structures, in particular the MO membrane and extracellular sheath, could serve as a physical boundary to constrain this positive feedback and control the overall shape/size of the MOs. This point is supported by the observation that in the *nompA* mutants, where the extracellular contact of the MOs is lost, the morphology of the MOs is largely altered (Fig. 7 A). Based on these considerations, we conclude that DCX-EMAP acts as a core ultrastructural organizer for the MOs of fly ciliated mechanoreceptors.

The implications on the roles of DCDCs in ciliary assembly

The functions of other DCDCs have also been implicated in cilia assembly and ciliopathy. For example, a missense mutation in *dcdc2*, which encodes DCDC2, causes human recessive deafness (Grati et al., 2015), likely by interfering with the structures of sensory hair cells and the supporting cells. Similar to DCX-EMAP, DCDC2 has a tandem pair of DCX domains at the amino terminus and an unstructured tail of over 200 residues at the carboxyl terminus, where the pathogenetic mutation is. Moreover, it also tends to localize to the distal end of cilia, similar to DCX-EMAP. Although the cellular functions and working mechanism of DCDC2 still await further studies, the expression of the deaf mutant of DCDC2 leads to disrupted ciliary structure, such as cilium branching and dysregulation of ciliary length, suggesting that DCDC2 has an essential role in organizing ciliary structures. This is to some extent similar to the function of DCX-EMAP in fly mechanosensory cilia. The resemblance in the cell biological features of DCDC2 and DCX-EMAP may suggest a common way of how DCDCs work in regulating ciliary structure, e.g., the ciliary tip compartment.

Materials and methods

Flies

Fly stocks used in this study were cultured on the standard medium and kept at 23–25°C. *w¹¹¹⁸* strain was used as *wild type*. *nompC³* strain was provided by Martin Göpfert (University of

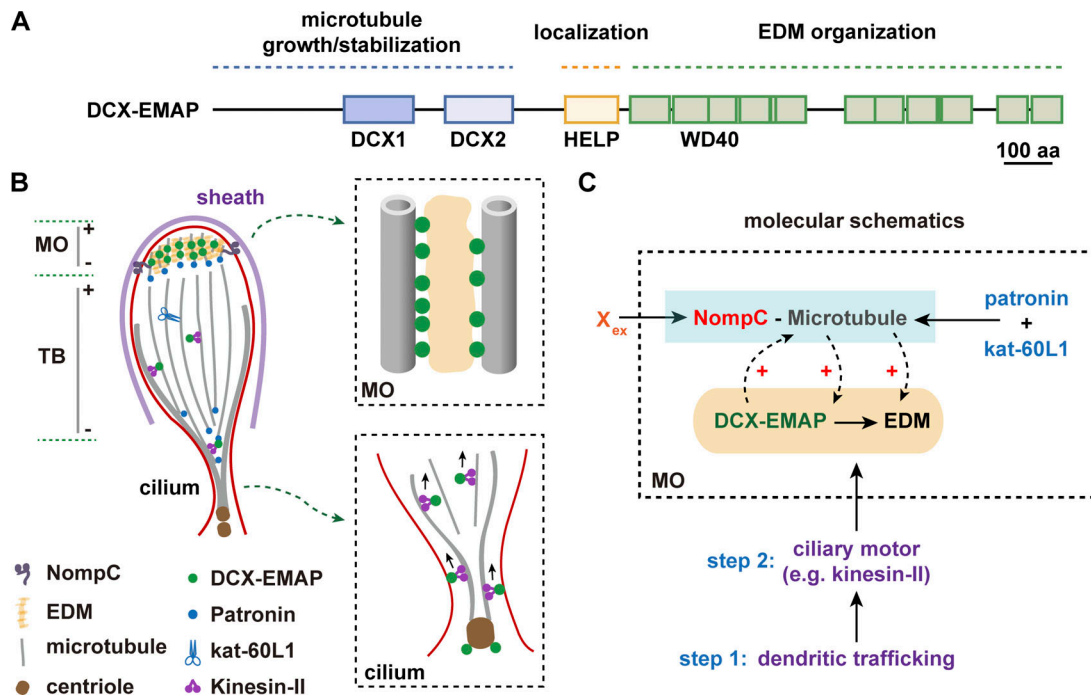


Figure 8. **Molecular mechanism underlying the formation of the MOs.** (A) Schematic diagram showing the domains of DCX-EMAP and their molecular functions. (B) Molecular organization of the microtubule-based cytoskeleton in the outer segment. Upper inset, molecular organization of the microtubules and EDMs in the MO. Lower inset, the molecular basis of ciliary transport of DCX-EMAP. (C) The molecular mechanism underlying the functions of DCX-EMAP in the formation of the MOs. X_{ex} : Extracellular factor that regulates the localization of NompC.

Göttingen, Göttingen, Germany). *nompC-gal4* and *uas-nompC-gfp* were provided by Wei Zhang (Tsinghua University, Beijing, China). *Dsas4^{s2214}* (BDSC 12119) was provided by Jingyan Fu (China Agricultural University, Beijing, China; Basto et al., 2006). *Cep290-GFP* strain was provided by Qing Wei (Wu et al., 2020). *Kat-60L^{BE6}* was provided by Nina Tang Sherwood (Duke University, Durham, NC, USA; Stewart et al., 2012). The *nompA¹* and *nompA²* strains were provided by Yun Doo Chung (University of Seoul, Seoul, Korea; originally from Maurice Kernan, The State University of New York, USA; Chung et al., 2001). *c01236* (BDSC 10430), *uas-gfp- α Tub84B* (BDSC 7374), *uas-Eb1-gfp* (BDSC 35512), *uas-p-gfp-cnn1* (BDSC 7255), *Klp64Dⁱ⁻⁴⁰⁹⁴⁵* (BDSC 40945), *uas-cd4-tdgfp* (BDSC 35836), *uas-cd4-tdTom* (BDSC 35841), and *uas-GCamp6s* (BDSC 42746) were from Bloomington stock centers. *DCX-EMAP-gal4*, *uas-cd4-tdtom*, *uas-mcherry- α Tub84B*, *uas-DCX-EMAP*, *nompC^{KI}*, and *Patronin^{KI}* were generated in our group (Sun et al., 2021).

DCX-EMAP^{KO} and *DCX-EMAP^{KI}* were generated using the CRISPR/Cas9-based strategy (Gratz et al., 2014). To knock out *DCX-EMAP*, two homologous arms (2 and 2.2 kb) corresponding to the 5' and 3' termini of the *DCX-EMAP* gene were cloned as the flanking regions for the 3P3-RFP cassette (i.e., the pMV-DCX-EMAP-HR construct). Four independent sgRNAs (KO-sgRNA1-4, see Table S1) were designed for a clean gene knockout of *DCX-EMAP* and used to yield pU6b-DCX-EMAP-KO-sgRNA (Ren et al., 2013). The pMV-DCX-EMAP-HR donor vector and the sgRNA-containing construct (pU6b-DCX-EMAP-KO-sgRNA) were co-injected into the embryos of *nos-Cas9-attp2* strain. The progenies with RFP markers were selected and further screened using a

polymerase chain reaction. To generate the *GFP-DCX-EMAP-KI* donor cassette, we amplified two 1.9-kb homologous arm sequences, one at the upstream 2 kb and the other at the 5' end of *DCX-EMAP*, respectively, from fly genomic DNA. This cassette was inserted into the pMV-donor vector. For higher efficiency, we designed two sgRNA for each recombinant site (KI-sgRNA1-4, see Table S1) and cloned them into the U6b-driven vector (i.e., pU6b-DCX-EMAP-KI-sgRNA). Then, the donor and sgRNA-containing constructs (pU6b-DCX-EMAP-KI-sgRNA) were injected into the embryos of the *nos-Cas9-attp2* strain. Progenies that were confirmed using PCR and had no obvious defects were used for further experiments.

To generate the *uas-gfp-DCX-EMAP* strain, the coding sequence of *DCX-EMAP* was cloned into the pTGW vector (*Drosophila* Gateway Collection). This approach was also used to generate other strains that expressed the mutant proteins of *DCX-EMAP*, such as Δ DCX1/2 (residues 166–380 deleted), Δ DCX1 (residues 166–255 deleted), Δ DCX2 (residues 295–380 deleted), Δ HELP (residues 448–514 deleted), and Δ WD40 (residues 575–1,076 deleted). The sequences for all the primers were provided (Table S1).

High-pressure freezing and freeze substitution

High-pressure freezing fixation of *Drosophila* legs and halteres was performed as previously described (Sun et al., 2021). Briefly, the dissected fly tissues were infiltrated in 0.1 M phosphate buffer. Then, the sample was inhaled into a cellulose capillary tube (16706869; Leica) and loaded into a 100- μ m-deep membrane carrier (16707898; Leica) that was filled with 20% BSA

aqueous solution and 0.05% pluronic acid (wt/vol, P2443; Sigma-Aldrich). The membrane carriers were sealed and cryo-immobilized using the high-pressure freezer (EM HPM100; Leica) and stored under liquid nitrogen.

During freeze substitution, the membrane carriers with frozen tissues were transferred into liquid nitrogen pre-cooled anhydrous acetone (10015; Electron Microscopy Sciences [EMS]) containing 1% osmium tetroxide (OsO₄; 19110; EMS), 0.1% uranyl acetate (21447; Polysciences), 0.5% glutaraldehyde (16220; EMS), and 4% pure water. Freeze substitution was carried out using a Leica EMAFS2 automatic freeze substitution device (Leica). The frozen samples were kept at -90°C for 40 h, warmed up at a rate of 5°C per hour, incubated at -30°C for 8 h, and finally warmed up at the rate of 5°C per hour to 0°C. After the substitution step, the samples were sequentially washed with ice-precooled anhydrous acetone and infiltrated with 1:3, 1:1, and 3:1 mixtures of Araldite-Epon (13940; EMS) and anhydrous acetone for 1 h at each step, followed by 100% Araldite-Epon infiltration overnight at room temperature. Finally, the samples with fresh Araldite-Epon were polymerized at 60°C for 48 h.

Electron tomography

The sections (250 nm) were acquired using a Leica EM UC7 ultramicrotome (Leica) and collected on Formvar-coated copper slot grids, as previously described (Sun et al., 2021). After that, staining was performed with 2% uranyl acetate in 70% methanol and then with 0.4% lead citrate (17900; EMS). Commercial 15-nm gold particles (EMGC15; BBI Solutions) were added to both sides of the sections as fiducial markers. Dual tilt-axis series ranging from -60° to +60° were collected using an FEI Tecnai F20 electron microscope (Thermo Fisher Scientific), which was equipped with a Gatan US4000 (895) CCD camera and controlled with the FEI Xplore 3D TEM tomography software.

Serial block-face imaging using FIB/SEM

The sample preparation for the serial block-face imaging was similar to that of electron tomography except for the embedding medium (44610; Durcupan™ ACM; Sigma-Aldrich). For serial FIB milling and SEM imaging, a layer of block surface was milled by a gallium ion beam, and the block face surface was imaged using an electron beam with 2 kV acceleration voltages, 0.4 nA current, and 8 μs dwell time on an FEI Helios NanoLab G3 UC FIB-SEM. After volume data collection, the images were imported into Amira (Thermo Fisher Scientific), aligned using the Dual-Beam 3D Wizard module, and exported as a stack of images in TIF format. The image stacks were then used for structural segmentation.

Structure reconstruction, segmentation, and measurement

Tomograms were reconstructed using the IMOD software package (v4.7; Mastronarde, 1997). The structural segmentation and three-dimensional surface generation for both ET and FIB-SEM data were performed in Amira (Thermo Fisher Scientific). All structural measurements in 3D space were performed in Amira.

Confocal imaging and photo bleaching

To image the expression pattern of DCX-EMAP, the tissue samples were imaged using a laser-scanning confocal microscope (LSM 780; Zeiss) equipped with a 63× oil UV-VIS-IR Apochromat objective (NA 1.2) at 25°C. To define the localization of DCX-EMAP, the fly halteres were imaged using a superresolution microscope (LSM980; Zeiss, Airyscan 2) equipped with a 63× oil Plan-Apochromat objective (NA 1.4; optical resolution: 120 nm) at 25°C. All the other optical microscopy data were collected using an Andor spinning disk confocal microscope (Andor) equipped with an inverted microscope (IX73; Olympus), an iXon 897 EMCCD, and a 100× UPlanSApo objective (NA 1.40; Olympus) at 25°C. The image acquisition software was Andor IQ 3.0 (Andor). The photobleaching experiments were performed using the Andor Frappa Unit (Andor) coupled to the spinning disk microscope. The fluorescence recovery (R_{rec} , in percentage) was calculated as

$$R_{rec} = \frac{F_t - F_0}{F_{-1} - F_0} \times 100\%$$

where F_{-1} is the fluorescence signal of the target region before bleaching, F_0 is the signal right after bleaching, and F_t is the recovered signal after a period (t).

Force-evoked calcium response in leg receptors

To record the mechanosensory responses of adult flies, we recorded the force-evoked neuronal increase of calcium signals in fly leg receptors. In brief, the adult fly (2–3 d old) expressing GCaMP6s calcium indicators in fly mechanoreceptors was immobilized on a 35-mm glass bottom dish. The legs were kept extended using double-sided tape. A piezo actuator (PZT 150/7/60 VS12; SuZhou Micro Automation Technology Co., Ltd) mounted with a glass probe (spherical tip, 60 μm in diameter) was used to apply mechanical stimulation (20 μm step) onto the outer segment of fly leg mechanoreceptors. The change of calcium signal (soma) in response to the mechanical stimuli was recorded using a spinning disk confocal microscope equipped with a 60× UPlanSApo objective (NA 1.40; Olympus). The amplitude of the calcium signal was measured to quantify the force-evoked responses.

Molecular biology

Total fly RNA was extracted using the RNeasy kit (Qiagen). The cDNA was synthesized using the SuperScript III Reverse Transcriptase (RT; Thermo Fisher Scientific). All PCR experiments were performed using the Golden Star T6 Super PCR Mix (TsingKe Biological Technology).

Flight test

Flight tests were performed as previously described (Bechstedt et al., 2010). Adult flies (2–3 d) without physical defects were allowed to recover from CO₂ overnight. Standard cylinders coated with paraffin oil (HZB0964-500; Harvey) were used. Fly vials were turned upside down in a funnel through which flies can fly into the cylinder. When the flies hit the wall of the cylinder, they would get stuck on the wall. The landing positions of all the flies were recorded and then used for statistical analysis.

Crawling test

Adult flies (2–3 d) were used for the crawling assay. For each movie recording, one fly was allowed to move in a mating plate (11-mm diameter). The continuous crawling behavior (30 s) was recorded using a 4K camera (FDR-AX60; SONY). The movies were analyzed using MATLAB (Mathworks), and the crawling speed was calculated.

Olfactory behavior test

Adult flies (2–3 d) were used for the olfactory behavior test using the olfactory aversive conditioning procedures (Gao et al., 2019). Flies were allowed to acclimate to the behavioral room at 25°C and 60% relative humidity for at least 30 min before the experiments. A group of about 100 flies were transferred to a T-maze and allowed to choose between odor A and odor B for 2 min. In our experiments, odor A was heavy mineral oil (O122-4; Fisher Chemical) and odor B was ethyl acetate (EA, Alfa Aesar) diluted in heavy mineral oil (20 μ l EA in 10 ml mineral oil). Performance index (PI) was calculated from the distribution of flies in the T-maze as

$$PI = (Fraction_A - Fraction_B) \times 100.$$

Immunostaining

Fly tissues were freshly collected in PBT (PBS with 0.5% Triton X-100) and then fixed in 4% paraformaldehyde (P6148; Sigma-Aldrich) augmented with 0.5% Triton X-100 (X100; Sigma-Aldrich) for 1 h. Then, the fixed samples were incubated with the primary antibody (20 μ g/ml for purified mouse monoclonal antibody against DCX-EMAP; Liang et al., 2014) overnight at 4°C. The next day, the samples were washed six times in PBS (5 min each time) and then incubated in the Alexa-conjugated secondary antibody (A32727; 1:200 dilution; Thermo Fisher Scientific) overnight at 4°C. On the third day, the samples were washed six times in PBS (5 min each time) and imaged using an Andor spinning disk confocal microscope (Andor) equipped with an inverted microscope (IX73; Olympus), an iXon 897 EMCCD, and a 100 \times UPlanSApo objective (NA 1.40; Olympus) at 25°C. The image acquisition software was Andor IQ 3.0 (Andor).

The single-nucleus transcriptomic atlas analysis

We explored the expression of DCX-EMAP in FlyCellAtlas (Li et al., 2022). Because the sequencing depth of SMART-seq2 is deeper than that of 10 \times Genomics, we chose the datasets generated by using the SMART-seq2 technology. The datasets for haltere, antenna, and leg were used in the present study. The expression profiles with UMAP algorithm were visualized using the Python package SCANPY (version 1.7.2; Wolf et al., 2018).

S2 cell transfection

S2 cells were cultured in the SIM SF Expression medium (SiniBiology) at 27°C. The coding sequences of DCX-EMAP, Δ DCX1/2 (residues 166–380 deleted), and Δ WD40 (residues 575–1,076 deleted) were subcloned into the Gateway pENTR/D-TOPO vector (Invitrogen) and finally into the destination vector pAGW or pAMW (DGRC). For transfection, 1 μ g plasmid was added into 100 μ l medium, followed by the addition of 10 μ l

FuGene HD Transfection Reagent (E2311; Promega) at a 2:1 (FuGene/DNA) ratio. Finally, the transfection mixture was then incubated at room temperature for 15 min and added to 1×10^6 cells seeded in a 12-well plate (Corning).

Multiple sequence alignment and protein structure prediction

Multiple sequence alignment was performed using ClustalX 2.1 (<http://www.clustal.org/clustal2/>). The structure models of the DCX tandem of DCX-EMAP (UniProt: Q9VUI3), human DCX (UniProt: O43602), and EML2S (UniProt: O95834) were predicted using the AlphaFold Protein Structure Database (<https://alphafold.com>). Model presentation was performed using PyMOL (version 2.5).

Protein expression and purification

The DCX1/2, DCX1, and DCX2 fragments of DCX-EMAP were expressed in *BL21E. coli* strain and purified using the Ni Sepharose columns (30210; QIAGEN). DCX1/2 and DCX1 were purified and stored in Tris-HCl buffer. DCX2 was purified and stored in the BRB80 buffer. Briefly, the cells were lysed in 50 mM Tris-HCl or BRB80, 10% glycerol, 200 mM KCl, 1 mM DTT, 10 mM imidazole, and 0.1% Tween 20 at pH 8.0 (Tris-HCl) or pH 6.9 (BRB80). After ultrasonic crushing, the lysate was centrifuged at 60,000 rpm and 4°C for 45 min. The supernatant was filtered and applied to the Ni Sepharose column (30210; QIAGEN). The column was washed with the washing buffer (50 mM Tris-HCl or BRB80, 10% glycerol, 200 mM KCl, 1 mM DTT, and 20 mM imidazole at pH 8.0 or 6.9) and balanced with the working buffer of 3°C protease (50 mM Tris-HCl or BRB80, 10% glycerol, 200 mM KCl, 1 mM DTT, and 10 mM imidazole at pH 8.0 or 6.9). His-tag was then removed on the Ni Sepharose column using 3°C protease (20409ES60; YEASEN; incubation overnight, 4°C). The eluted protein was further purified using the Source Q anion exchange column (GE Healthcare Life Sciences) and the Superdex 200 column (SD200; GE Healthcare Life Sciences). The purified protein was analyzed using SDS-PAGE (Coomassie blue staining) and stored in the storage buffer (50 mM Tris-HCl or BRB80, 10% glycerol, 200 mM KCl, and 1 mM DTT at pH 8.0 or 6.9).

Tubulin purification and in vitro MT dynamic assay

Drosophila S2 tubulin was purified using the TOG-based affinity column as previously described (Gell et al., 2011; Widlund et al., 2012). One step of the polymerization/depolymerization cycle was followed to further improve the activity and purity of tubulin. Tubulin labeling experiments with TAMRA (C1171; Thermo Fisher Scientific) and Alexa Fluor 647 (A20106; Thermo Fisher Scientific) were performed according to the standard protocols (Gell et al., 2010, 2011). The in vitro microtubule dynamic assay was performed as previously described (Gell et al., 2010; Song et al., 2020). Briefly, in a flow cell, GMPCPP (NU-405L; Roche)-stabilized microtubules (30% biotin and 5% Alexa Fluor 647 labeled) were attached to the coverslip coated with biotin-binding proteins (31000; Thermo Fisher Scientific). Free tubulin dimer (10% TAMRA labeled) in the reaction buffer (BRB80 supplemented with 50 mM KCl, 1 mM MgCl₂, 80 mM D-glucose, 0.4 mg/ml glucose oxidase, 0.16 mg/ml catalase,

0.8 mg/ml casein, 1% β -mercaptoethanol, 0.001% Tween 20, 0.15% sodium carboxymethylcellulose, and 2 mM GTP) was then added into the flow cell. Dynamic microtubules can be recorded using a total internal reflection fluorescence (TIRF) microscope (Olympus, Japan) equipped with an Andor 897 Ultra EMCCD camera (Andor) and a 100 \times TIRF objective (NA 1.49; Olympus).

Quantification and statistical analysis

Data quantification and statistical analysis were performed using OriginPro 8.5 (OriginLab Corporation) and MATLAB R2018b (MathWorks). Box plots were shown with lower quartiles, median (line in the box), mean (circle), and upper quartile. Statistical analysis was performed using the two-sided unpaired Student's *t* test. Data distribution was assumed to be normal, but this was not formally tested.

Image analysis

Fluorescence signal measurements

For the measurement of fluorescent signal (e.g., GFP-DCX-EMAP), the regions of interest were first selected and then the fluorescent intensity of these regions was measured using Fiji (Schindelin et al., 2012).

Microtubule density

To measure the density of microtubules in ET volume data, the area of target regions was measured and the number of microtubules in this region was counted using Amira 6.0 (Thermo Fisher Scientific). The density was calculated as the number of microtubules divided by the area.

Online supplemental material

Fig. S1 shows the 3D porous structure of EDMs and their direct deposition on the microtubule wall. **Fig. S2** shows the expression of DCX-EMAP in fly mechanosensory organs and olfactory receptor cells. **Fig. S3** shows the single-nucleus transcriptomic atlas of DCX-EMAP. **Fig. S4** shows the ultrastructure of the outer segment of the haltere receptors in wild type and DCX-EMAPKO. **Fig. S5** shows the working mechanism of the DCX domain in DCX-EMAP. **Table. S1** shows the sequences for the primers and oligos used in the present study. **Video 1** shows the volume data of the OS in a haltere campaniform mechanoreceptor. **Video 2** shows the volume data of the OS in a leg campaniform mechanoreceptor. **Video 3** shows the crawling behaviors of wild type, DCX-EMAPKO, and rescue-1. **Video 4** shows the FIB-SEM volume data of the OS of a haltere campaniform mechanoreceptor in wild type or DCX-EMAPKO. **Video 5** shows the volume data of the MO of a haltere campaniform mechanoreceptor in DCX-EMAPKO. **Video 6** shows the volume data of the TB of a haltere campaniform mechanoreceptor in DCX-EMAPKO. **Video 7** shows the volume data of the OS of a leg campaniform mechanoreceptor in DCX-EMAPKO. **Video 8** shows the volume data of the OS of a leg campaniform mechanoreceptor in Δ DCX1/2rescue. **Video 9** shows the volume data of the OS of a leg campaniform mechanoreceptor in Δ WD40rescue. **Video 10** shows the crawling behaviors of various rescue strains of DCX-EMAP.

Data availability

All data underlying the research presented in the manuscript are available in the article itself, its supplementary materials, or from the authors, upon reasonable request.

Acknowledgments

The authors thank Martin Göpfert, Wei Zhang, Jingyan Fu, Wei Qing, Nina Tang Sherwood, Yun Doo Chung, Maurice Kernan, and the Jan lab for sharing fly strains. We thank Jianjian Zhao from Yi Zhong Group (Tsinghua University) and Jing-Ru Yang for technical assistance. Special thanks to the electron microscopy facility and Cell Biology facility at Tsinghua University.

We acknowledge our funding from the National Natural Sciences Foundation of China (32070704 and 32370730), Tsinghua-Peking Center for Life Sciences, Beijing Advanced Innovation Center for Structural Biology, and IDG/McGovern Institute for Brain Research (Tsinghua University).

Author contributions: X. Song, L. Sun, and X. Liang designed experiments. X. Song, L. Cui, M. Wu, S. Wang, Z. Liu, Z. Xue, Y. Zhang, and H. Li performed the experiments. X. Song, Y. Song, and W. Chen analyzed data. X. Liang supervised the project. X. Song and X. Liang wrote and revised the manuscript, which was read and edited by all authors.

Disclosures: The authors declare no competing interests exist.

Submitted: 29 September 2022

Revised: 21 June 2023

Accepted: 9 August 2023

References

- Basto, R., J. Lau, T. Vinogradova, A. Gardiol, C.G. Woods, A. Khodjakov, and J.W. Raff. 2006. Flies without centrioles. *Cell*. 125:1375–1386. <https://doi.org/10.1016/j.cell.2006.05.025>
- Bechstedt, S., J.T. Albert, D.P. Kreil, T. Müller-Reichert, M.C. Göpfert, and J. Howard. 2010. A doublecortin containing microtubule-associated protein is implicated in mechanotransduction in Drosophila sensory cilia. *Nat. Commun.* 1:11. <https://doi.org/10.1038/ncomms1007>
- Bowne-Anderson, H., A. Hibbel, and J. Howard. 2015. Regulation of microtubule growth and catastrophe: unifying theory and experiment. *Trends Cell Biol.* 25:769–779. <https://doi.org/10.1016/j.tcb.2015.08.009>
- Brisch, E., M.A. Daggett, and K.A. Suprenant. 1996. Cell cycle-dependent phosphorylation of the 77 kDa echinoderm microtubule-associated protein (EMAP) in vivo and association with the p34cdc2 kinase. *J. Cell Sci.* 109:2885–2893. <https://doi.org/10.1242/jcs.109.12.2885>
- Chalfie, M. 2009. Neurosensory mechanotransduction. *Nat. Rev. Mol. Cell Biol.* 10:44–52. <https://doi.org/10.1038/nrm2595>
- Chung, Y.D., J. Zhu, Y. Han, and M.J. Kernan. 2001. nompA encodes a PNS-specific, ZP domain protein required to connect mechanosensory dendrites to sensory structures. *Neuron*. 29:415–428. [https://doi.org/10.1016/S0896-6273\(01\)00215-X](https://doi.org/10.1016/S0896-6273(01)00215-X)
- Deuel, T.A., J.S. Liu, J.C. Corbo, S.Y. Yoo, L.B. Rorke-Adams, and C.A. Walsh. 2006. Genetic interactions between doublecortin and doublecortin-like kinase in neuronal migration and axon outgrowth. *Neuron*. 49:41–53. <https://doi.org/10.1016/j.neuron.2005.10.038>
- Eichenmuller, B., P. Everley, J. Palange, D. Lepley, and K.A. Suprenant. 2002. The human EMAP-like protein-70 (ELP70) is a microtubule destabilizer that localizes to the mitotic apparatus. *J. Biol. Chem.* 277:1301–1309. <https://doi.org/10.1074/jbc.M106628200>
- Francis, F., A. Koulakoff, D. Boucher, P. Chafey, B. Schaar, M.C. Vinet, G. Friocourt, N. McDonnell, O. Reiner, A. Kahn, et al. 1999. Doublecortin is a developmentally regulated, microtubule-associated protein expressed

- in migrating and differentiating neurons. *Neuron*. 23:247–256. [https://doi.org/10.1016/S0896-6273\(00\)80777-1](https://doi.org/10.1016/S0896-6273(00)80777-1)
- Fry, A.M., L. O'Regan, J. Montgomery, R. Adib, and R. Bayliss. 2016. EML proteins in microtubule regulation and human disease. *Biochem. Soc. Trans.* 44:1281–1288. <https://doi.org/10.1042/BST20160125>
- Gao, Y., Y. Shuai, X. Zhang, Y. Peng, L. Wang, J. He, Y. Zhong, and Q. Li. 2019. Genetic dissection of active forgetting in labile and consolidated memories in *Drosophila*. *Proc. Natl. Acad. Sci. USA*. 116:21191–21197. <https://doi.org/10.1073/pnas.1903763116>
- Gell, C., V. Bormuth, G.J. Brouhard, D.N. Cohen, S. Diez, C.T. Friel, J. Helenius, B. Nitzsche, H. Petzold, J. Ribbe, et al. 2010. Microtubule dynamics reconstituted in vitro and imaged by single-molecule fluorescence microscopy. 95:221–245. [https://doi.org/10.1016/S0091-679X\(10\)95013-9](https://doi.org/10.1016/S0091-679X(10)95013-9)
- Gell, C., C.T. Friel, B. Borgonovo, D.N. Drechsel, A.A. Hyman, and J. Howard. 2011. Purification of tubulin from porcine brain. *Methods Mol. Biol.* 777: 15–28. https://doi.org/10.1007/978-1-61779-252-6_2
- Gillespie, P.G., and U. Müller. 2009. Mechanotransduction by hair cells: Models, molecules, and mechanisms. *Cell*. 139:33–44. <https://doi.org/10.1016/j.cell.2009.09.010>
- Gillespie, P.G., and R.G. Walker. 2001. Molecular basis of mechanosensory transduction. *Nature*. 413:194–202. <https://doi.org/10.1038/35093011>
- Gleeson, J.G., P.T. Lin, L.A. Flanagan, and C.A. Walsh. 1999. Doublecortin is a microtubule-associated protein and is expressed widely by migrating neurons. *Neuron*. 23:257–271. [https://doi.org/10.1016/S0896-6273\(00\)80778-3](https://doi.org/10.1016/S0896-6273(00)80778-3)
- Goodman, M.B. 2006. Mechanosensation. *WormBook*. 6:1–14. <https://doi.org/10.1895/wormbook.1.62.1>
- Goodwin, S.S., and R.D. Vale. 2010. Patronin regulates the microtubule network by protecting microtubule minus ends. *Cell*. 143:263–274. <https://doi.org/10.1016/j.cell.2010.09.022>
- Grati, M., I. Chakchouk, Q. Ma, M. Bensaïd, A. Desmidt, N. Turki, D. Yan, A. Baanannou, R. Mittal, N. Driss, et al. 2015. A missense mutation in DCDC2 causes human recessive deafness DFNB66, likely by interfering with sensory hair cell and supporting cell cilia length regulation. *Hum. Mol. Genet.* 24:2482–2491. <https://doi.org/10.1093/hmg/ddv009>
- Gratz, S.J., F.P. Ukken, C.D. Rubinstein, G. Thiede, L.K. Donohue, A.M. Cummings, and K.M. O'Connor-Giles. 2014. Highly specific and efficient CRISPR/Cas9-catalyzed homology-directed repair in *Drosophila*. *Genetics*. 196:961–971. <https://doi.org/10.1534/genetics.113.160713>
- Hamill, D.R., B. Howell, L. Cassimeris, and K.A. Suprenant. 1998. Purification of a WD repeat protein, EMAP, that promotes microtubule dynamics through an inhibition of rescue. *J. Biol. Chem.* 273:9285–9291. <https://doi.org/10.1074/jbc.273.15.9285>
- Hendershott, M.C., and R.D. Vale. 2014. Regulation of microtubule minus-end dynamics by CAMSAPs and Patronin. *Proc. Natl. Acad. Sci. USA*. 111: 5860–5865. <https://doi.org/10.1073/pnas.1404133111>
- Hotta, T., T.S. McAlear, Y. Yue, T. Higaki, S.E. Haynes, A.I. Nesvizhskii, D. Sept, K.J. Verhey, S. Bechtold, and R. Ohi. 2022. EML2-S constitutes a new class of proteins that recognizes and regulates the dynamics of tyrosinated microtubules. *Curr. Biol.* 32:3898–3910.e14. <https://doi.org/10.1016/j.cub.2022.07.027>
- Howard, J. 2001. *Mechanics of Motor Proteins and the Cytoskeleton*. Sinauer Associates, Publishers, Sunderland, MA.
- Hueston, J.L., G.P. Herren, J.G. Cueva, M. Buechner, E.A. Lundquist, M.B. Goodman, and K.A. Suprenant. 2008. The *C. elegans* EMAP-like protein, ELP-1 is required for touch sensation and associates with microtubules and adhesion complexes. *BMC Dev. Biol.* 8:110. <https://doi.org/10.1186/1471-213X-8-110>
- Keil, T.A. 1997. Functional morphology of insect mechanoreceptors. *Microsc. Res. Tech.* 39:506–531. [https://doi.org/10.1002/\(SICI\)1097-0029\(19971215\)39:6<506::AID-JEMT5>3.0.CO;2-B](https://doi.org/10.1002/(SICI)1097-0029(19971215)39:6<506::AID-JEMT5>3.0.CO;2-B)
- Li, H., J. Janssens, M. De Waegeneer, S.S. Kolluru, K. Davie, V. Gardeux, W. Saelens, F.P.A. David, M. Brbić, K. Spanier, et al. 2022. Fly cell atlas: A single-nucleus transcriptomic atlas of the adult fruit fly. *Science*. 375: eabk2432. <https://doi.org/10.1126/science.abk2432>
- Liang, X., J. Madrid, R. Gärtner, J.M. Verbavatz, C. Schiklenk, M. Wilsch-Bräuninger, A. Bogdanova, F. Stenger, A. Voigt, and J. Howard. 2013. A NOMPC-dependent membrane-microtubule connector is a candidate for the gating spring in fly mechanoreceptors. *Curr. Biol.* 23:755–763. <https://doi.org/10.1016/j.cub.2013.03.065>
- Liang, X., J. Madrid, and J. Howard. 2014. The microtubule-based cytoskeleton is a component of a mechanical signaling pathway in fly campaniform receptors. *Biophys. J.* 107:2767–2774. <https://doi.org/10.1016/j.bpj.2014.10.052>
- Lumpkin, E.A., K.L. Marshall, and A.M. Nelson. 2010. The cell biology of touch. *J. Cell Biol.* 191:237–248. <https://doi.org/10.1083/jcb.201006074>
- Manka, S.W., and C.A. Moores. 2020. Pseudo-repeats in doublecortin make distinct mechanistic contributions to microtubule regulation. *EMBO Rep.* 21:e51534. <https://doi.org/10.15252/embr.202051534>
- Mastronarde, D.N. 1997. Dual-axis tomography: An approach with alignment methods that preserve resolution. *J. Struct. Biol.* 120:343–352. <https://doi.org/10.1006/jsbi.1997.3919>
- Moores, C.A., M. Perderiset, F. Francis, J. Chelly, A. Houdusse, and R.A. Milligan. 2004. Mechanism of microtubule stabilization by doublecortin. *Mol. Cell*. 14:833–839. <https://doi.org/10.1016/j.molcel.2004.06.009>
- Moores, C.A., M. Perderiset, C. Kappeler, S. Kain, D. Drummond, S.J. Perkins, J. Chelly, R. Cross, A. Houdusse, and F. Francis. 2006. Distinct roles of doublecortin modulating the microtubule cytoskeleton. *EMBO J.* 25: 4448–4457. <https://doi.org/10.1038/sj.emboj.7601335>
- Pollmann, M., R. Parwaresch, S. Adam-Klages, M.L. Kruse, F. Buck, and H.J. Heidebrecht. 2006. Human EML4, a novel member of the EMAP family, is essential for microtubule formation. *Exp. Cell Res.* 312:3241–3251. <https://doi.org/10.1016/j.yexcr.2006.06.035>
- Ren, X., J. Sun, B.E. Housden, Y. Hu, C. Roesel, S. Lin, L.P. Liu, Z. Yang, D. Mao, L. Sun, et al. 2013. Optimized gene editing technology for *Drosophila melanogaster* using germ line-specific Cas9. *Proc. Natl. Acad. Sci. USA*. 110:19012–19017. <https://doi.org/10.1073/pnas.1318481110>
- Schindelin, J., I. Arganda-Carreras, E. Frise, V. Kaynig, M. Longair, T. Pietzsch, S. Preibisch, C. Rueden, S. Saalfeld, B. Schmid, et al. 2012. Fiji: An open-source platform for biological-image analysis. *Nat. Methods*. 9: 676–682. <https://doi.org/10.1038/nmeth.2019>
- Song, Y., Y. Zhang, Y. Pan, J. He, Y. Wang, W. Chen, J. Guo, H. Deng, Y. Xue, X. Fang, and X. Liang. 2020. The microtubule end-binding affinity of EBI is enhanced by a dimeric organization that is susceptible to phosphorylation. *J. Cell Sci.* 133:jcs241216. <https://doi.org/10.1242/jcs.241216>
- Stewart, A., A. Tsubouchi, M.M. Rolls, W.D. Tracey, and N.T. Sherwood. 2012. Katanin p60-like1 promotes microtubule growth and terminal dendrite stability in the larval class IV sensory neurons of *Drosophila*. *J. Neurosci.* 32:11631–11642. <https://doi.org/10.1523/JNEUROSCI.0729-12.2012>
- Sun, L., L. Cui, Z. Liu, Q. Wang, Z. Xue, M. Wu, T. Sun, D. Mao, J. Ni, J.C. Pastor-Pareja, and X. Liang. 2021. Katanin p60-like 1 sculpts the cytoskeleton in mechanosensory cilia. *J. Cell Biol.* 220:e202004184. <https://doi.org/10.1083/jcb.202004184>
- Sun, L., Y. Gao, J. He, L. Cui, J. Meissner, J.M. Verbavatz, B. Li, X. Feng, and X. Liang. 2019. Ultrastructural organization of NompC in the mechanoreceptive organelle of *Drosophila* campaniform mechanoreceptors. *Proc. Natl. Acad. Sci. USA*. 116:7343–7352. <https://doi.org/10.1073/pnas.1819371116>
- Vosshall, L.B., and R.F. Stocker. 2007. Molecular architecture of smell and taste in *Drosophila*. *Annu. Rev. Neurosci.* 30:505–533. <https://doi.org/10.1146/annurev.neuro.30.051606.094306>
- Wang, J., J. Jiang, X. Yang, G. Zhou, L. Wang, and B. Xiao. 2022. Tethering Piezo channels to the actin cytoskeleton for mechanogating via the cadherin- β -catenin mechanotransduction complex. *Cell Rep.* 38:110342. <https://doi.org/10.1016/j.celrep.2022.110342>
- Widlund, P.O., M. Podolski, S. Reber, J. Alper, M. Storch, A.A. Hyman, J. Howard, and D.N. Drechsel. 2012. One-step purification of assembly-competent tubulin from diverse eukaryotic sources. *Mol. Biol. Cell*. 23: 4393–4401. <https://doi.org/10.1091/mbc.e12-06-0444>
- Wolf, F.A., P. Angerer, and F.J. Theis. 2018. Scanpy: Large-scale single-cell gene expression data analysis. *Genome Biol.* 19:15. <https://doi.org/10.1186/s13059-017-1382-0>
- Wu, Z., N. Pang, Y. Zhang, H. Chen, Y. Peng, J. Fu, and Q. Wei. 2020. CEP290 is essential for the initiation of ciliary transition zone assembly. *PLoS Biol.* 18:e3001034. <https://doi.org/10.1371/journal.pbio.3001034>

Supplemental material

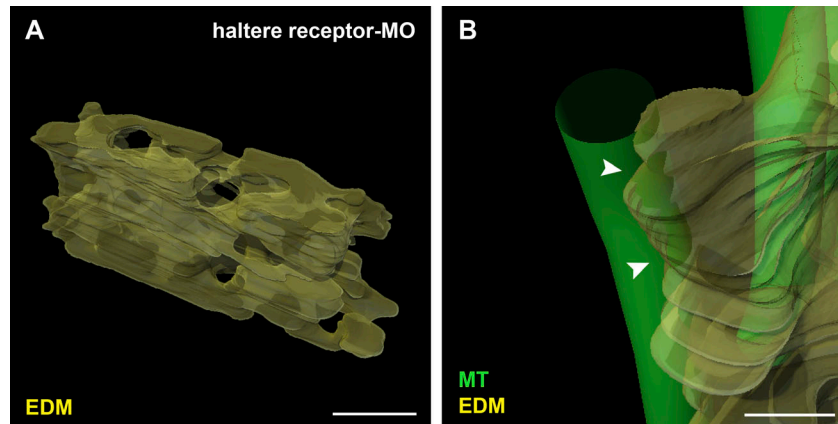


Figure S1. **The EDMs form a 3D porous structure and deposit on the wall of microtubules.** (A) Reconstructed model of the EDMs in the MO of a haltere receptor. Scale bar, 100 nm. (B) Enlarged image of a local region showing the direct deposition of the EDMs on the microtubule wall (white arrowheads). Scale bar, 20 nm.

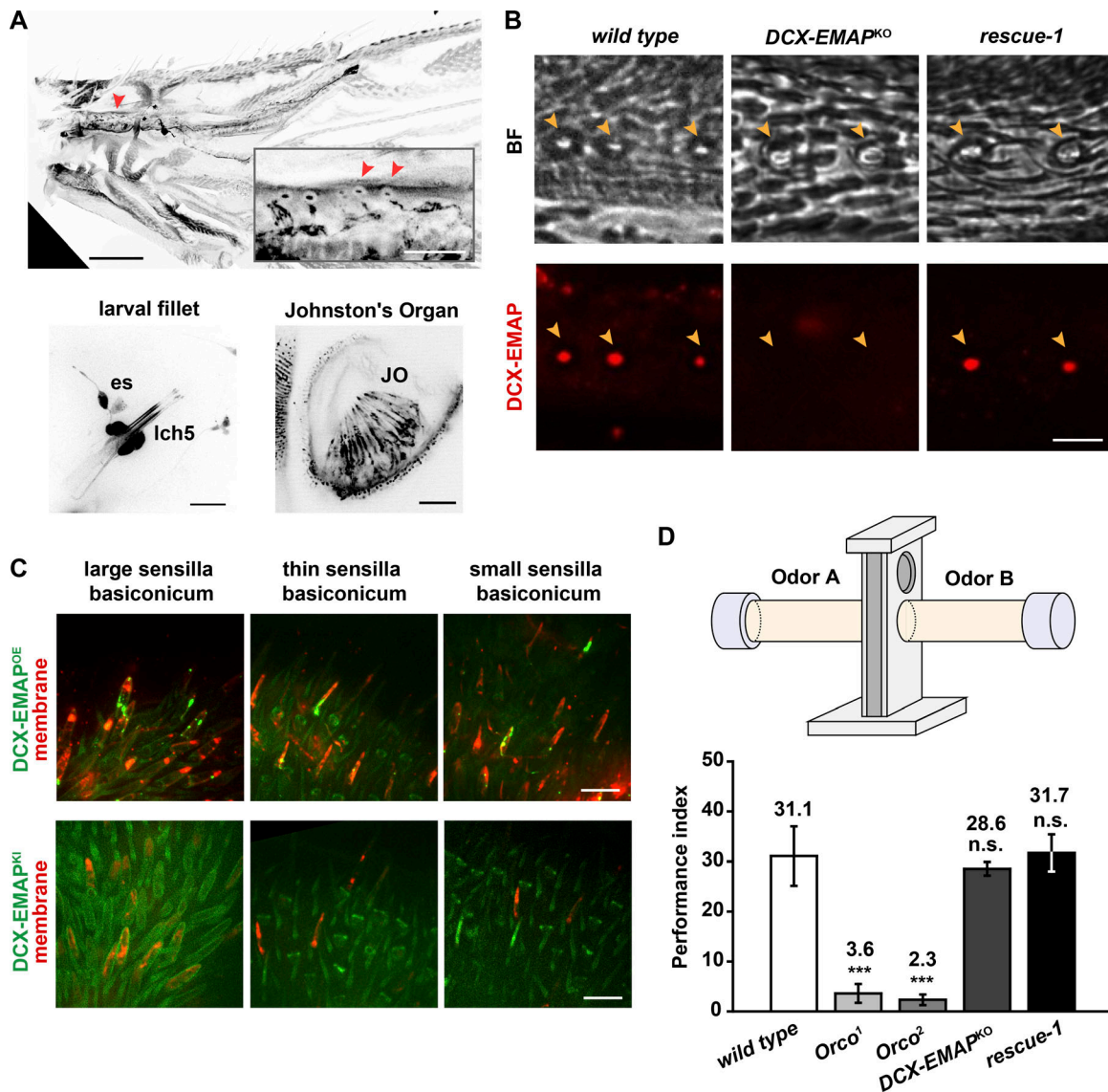
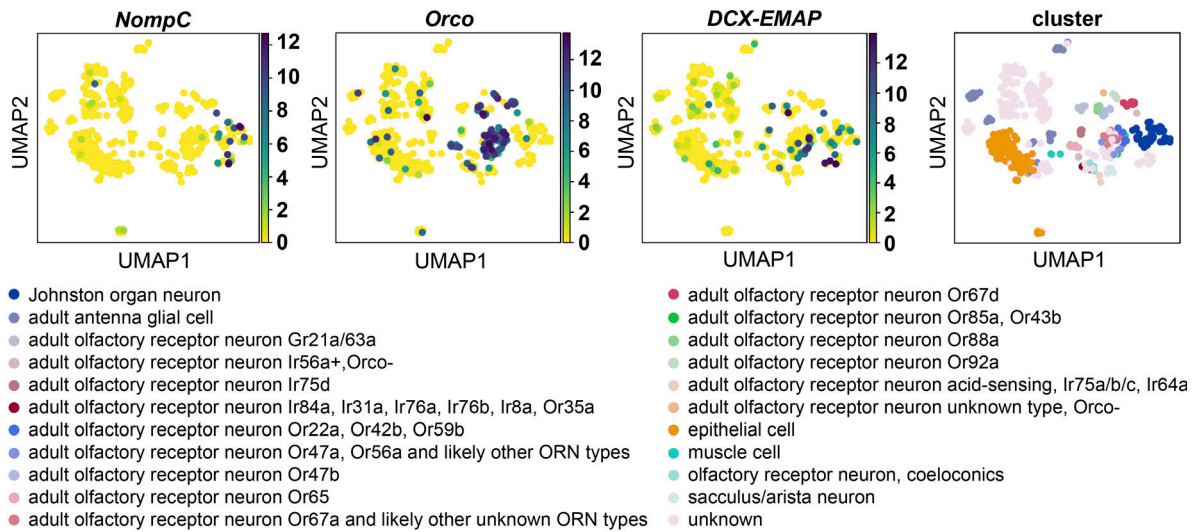
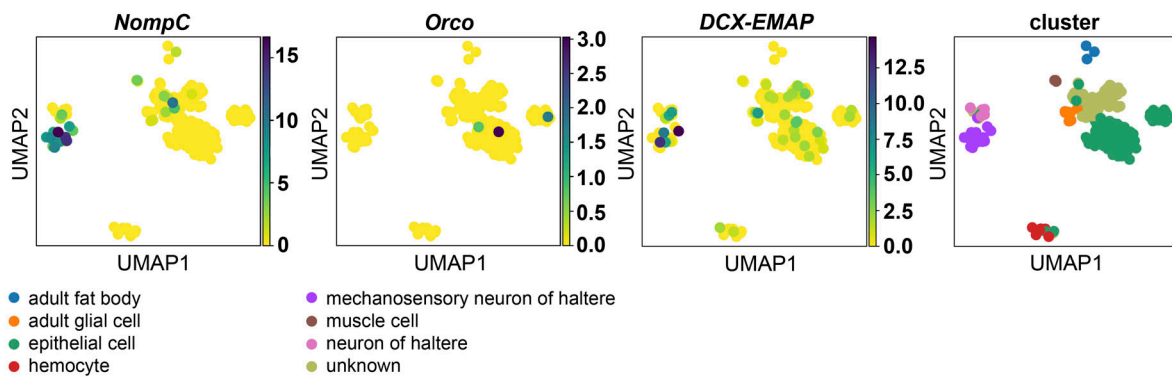


Figure S2. **The expression of DCX-EMAP in fly mechanosensory organs and olfactory receptor cells.** (A) The expression of DCX-EMAP (*DCX-EMAP-gal4; uas-cd4-tdgfp*) in the campaniform receptors at wing base (upper), larval lch5 (lower left), and the Johnson's organ (lower right) of adult fly. The red arrowheads mark the campaniform receptors. Upper panel: scale bar, 100 μ m; inset scale bar, 20 μ m. Lower panel: scale bar, 25 μ m. (B) Representative images showing the absence of the DCX-EMAP signal in *DCX-EMAP^{KO}* and the recovery of the signal in *DCX-EMAP^{rescue}* (*DCX-EMAP-gal4/uas-gfp-DCX-EMAP; DCX-EMAP^{KO}*) in the campaniform mechanoreceptors at the wing base. The immunofluorescence staining experiments were performed using the anti-DCX-EMAP antibody (Liang et al., 2014). The orange arrowheads indicate the campaniform receptors at the wing base. Scale bar, 5 μ m. (C) The subcellular localization of GFP-DCX-EMAP in the olfactory receptors of *DCX-EMAP^{KI}* (lower) and *DCX-EMAP^{OE}* (upper, *DCX-EMAP-gal4, uas-cd4-tdtom/uas-gfp-DCX-EMAP*) strains. Note that the localization of DCX-EMAP in *DCX-EMAP^{KI}* was not visible, while that in *DCX-EMAP^{OE}* appeared to be fragmentary. Scale bar, 10 μ m. Inset scale bar, 5 μ m. (D) Olfactory tests on *wild type* ($n = 730$ flies from seven assays), *Orco¹* ($n = 286$ flies from three assays), *Orco²* ($n = 326$ flies from three assays), *DCX-EMAP^{KO}* ($n = 299$ flies from three assays), and *DCX-EMAP^{rescue}* (*DCX-EMAP-gal4/uas-gfp-DCX-EMAP; DCX-EMAP^{KO}*, $n = 366$ flies from four assays). Two-sided unpaired Student's test. ***, $P < 0.001$; n.s., no significance. Note that *Orco*, also known as *Or83b*, encodes broadly expressed chemoreceptors in almost all fly olfactory organs (Vosshall and Stocker, 2007). *Orco¹* and *Orco²* are null mutants of *Orco*.

A antenna



B haltere



C leg

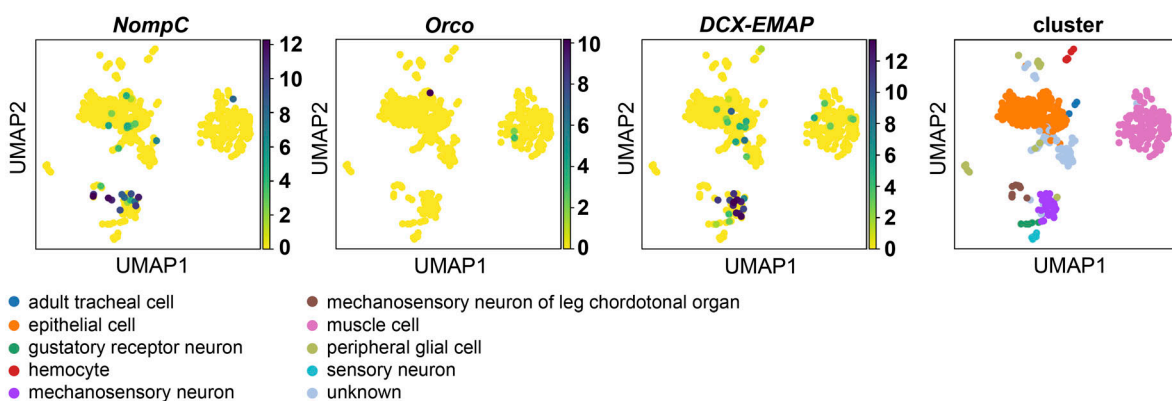


Figure S3. **The single-nucleus transcriptomic atlas of DCX-EMAP. (A-C)** The single-nucleus transcriptomic atlas of *NompC*, *Orco*, and *DCX-EMAP* in antenna (A), haltere (B), and leg (C) tissues. The datasets were from FlyCellAtlas (Li et al., 2022).

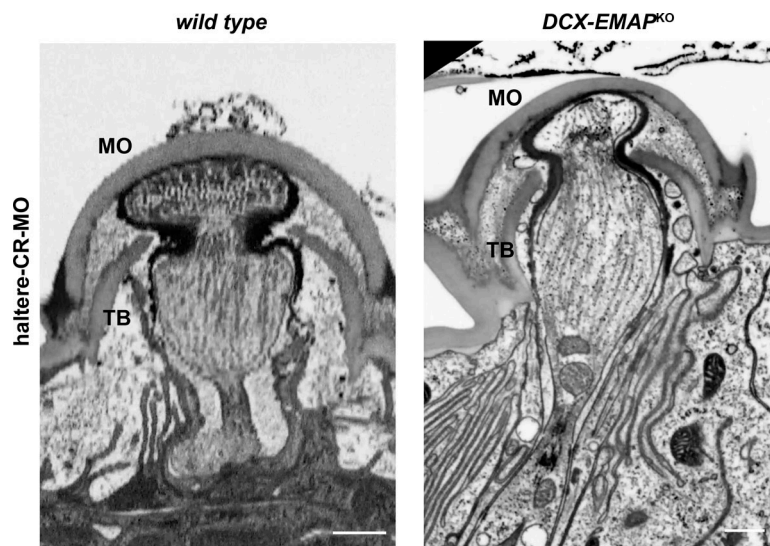


Figure S4. **DCX-EMAP is required for the ultrastructure of the MO.** Representative FIB-SEM images showing the ultrastructure of the outer segment of the haltere receptors in *wild type* (left panel) and *DCX-EMAP^{KO}* (right panel). Scale bar, 500 nm. Also see [Video 4](#).

Video 2. **The volume data of the OS in a leg campaniform mechanoreceptor (lateral view).** Scale bar, 300 nm.

Video 3. **The crawling behavior of wild type, DCX-EMAPKO, and rescue-1 (DCX-EMAP-gal4/uas-gfp-DCX-EMAP;DCX-EMAPKO).** The crawling trajectories were shown at the end of the movie.

Video 4. **The FIB-SEM volume data of the OS of a haltere campaniform mechanoreceptor in wild type or DCX-EMAPKO (lateral view).** Scale bar, 500 nm.

Video 5. **The volume data of the MO of a haltere campaniform mechanoreceptor in DCX-EMAPKO (cross-sectional view).** Scale bar, 200 nm.

Video 6. **The volume data of the TB of a haltere campaniform mechanoreceptor in DCX-EMAPKO (cross-sectional view).** Scale bar, 200 nm.

Video 7. **The volume data of the OS of a leg campaniform mechanoreceptor in DCX-EMAPKO (lateral view).** Scale bar, 200 nm.

Video 8. **The volume data of the OS of a leg campaniform mechanoreceptor in Δ DCX1/2rescue (lateral view).** Scale bar, 300 nm.

Video 9. **The volume data of the OS of a leg campaniform mechanoreceptor in Δ WD40rescue (lateral view).** Scale bar, 300 nm.

Video 10. **The crawling behavior of various rescue strains of DCX-EMAP.** The crawling trajectories were shown at the end of the movie.

Provided online is Table S1. Table S1 shows the primers/oligos used in the present study used in this study.